Multizone shell model for turbulent wall bounded flows

Victor S. L'vov, Anna Pomyalov, and Vasil Tiberkevich
Department of Chemical Physics, The Weizmann Institute of Science, Rehovot 76100, Israel
(Received 12 May 2003; published 28 October 2003)

We suggested a multizone shell (MZS) model for wall-bounded flows accounting for the space inhomogeneity in a piecewise approximation, in which the cross-sectional area of the flow, S, is subdivided into j zones. The area of the first zone, responsible for the core of the flow, $S_1 \simeq S/2$, and the areas of the next j zones, S_j, decrease toward the wall like $S_j \propto 2^{-j}$. In each j zone the statistics of turbulence is assumed to be space homogeneous and is described by the set of shell velocities $u_{nj}(t)$ for turbulent fluctuations of the scale proportional to 2^{-n}. The MZS model includes a set of complex variables $V_j(t)$, $j=1,2,\ldots,\infty$, describing the amplitudes of the near-wall coherent structures of the scale $s_j \sim 2^{-j}$ and responsible for the mean velocity profile. The suggested MZS equations of motion for $u_{nj}(t)$ and $V_j(t)$ preserve the actual conservation laws (energy, mechanical, and angular momenta), respect the existing symmetries (including Galilean and scale invariance), and account for the type of nonlinearity in the Navier-Stokes equation, dimensional reasoning, etc. The MZS model qualitatively describes important characteristics of the wall-bounded turbulence, e.g., evolution of the mean velocity profile with increasing Reynolds number Re from the laminar profile toward the universal logarithmic profile near the flat-plane boundary layer as $Re \to \infty$.

DOI: 10.1103/PhysRevE.68.046308 PACS number(s): 47.27.Nz, 05.45.−a, 47.27.Eq

I. INTRODUCTION

A. Background

Three simple turbulent flows—in a channel, in a pipe, and near a flat plane—play a prominent role in our understanding of spatially inhomogeneous wall-bounded flows, similar to the celebrated role of developed homogeneous turbulence in understanding the universal statistical behavior of fine-scale turbulence. Along the long road toward understanding homogeneous turbulence, there appeared various phenomenological cascade models of turbulence (the Richardson-Kolmogorov 1941 concept of turbulence and the Kolmogorov 1962 log-normal and multifractal models of intermittency), many closure procedures (like the Kraichnan direct interaction approximation), and various field theoretical approaches. Last but not least we have to mention the so-called shell models of turbulence (like the GOY shell model [1,2] together with its ''Sabra'' improvement [3], and many others [4]). For the recent development of shell models see the review by Biferale [5]. Separately, we want to mention Zimin's shell model ([22]; see also [6,7]), which was derived from the Navier-Stokes equation (NSE) using a vector wavelet decomposition [8] of the velocity field and involves no empirical or *ad hoc* parameters.

Shell models are systems of ordinary differential equations which mimic the statistically homogeneous isotropic turbulent velocity field in some interval of scales (say, within some ''shell'' in the Fourier space) by one or a few ''shell velocities'' $u_n(t)$ [4]. The shell models have the same (quadratic) type of nonlinearity as the NSE, respect the conservation of energy (in the unforced, inviscid limit), and have built-in locality of interaction of neighboring scales, reflecting scale-by-scale energy transfer toward dissipative scales. Surprisingly, the shell models allow us to mimic almost everything we know (experimentally, theoretically, or by direct numerical simulation) about highly nontrivial statistics of fine-scale turbulence. This includes, for instance, the intermittent behavior of the velocity structure functions (which are simultaneous, two-point nth-order correlation function of velocity differences), the fusion rules (which govern the asymptotic behavior of many-point velocity correlation functions), and so on. A possible reason for such a lucky success is that the above mentioned (and some other) characteristics of the turbulent statistics are robust and depend only on some very general physical requirements, such as respect for the actual conservation laws, scale invariance, the type of nonlinearity in the NSE, and the locality of interaction. All these features are accounted for in the shell models. There has been a set of important attempts to construct shell models with a real space structure [9–11].

Unfortunately, shell models in their traditional formulations describe only space homogeneous turbulence, leaving aside wall-bounded turbulence, which plays a much more important role in practical applications.

Turbulent flows at high Reynolds numbers $Re \gg 1$, contain such a wide range of excited lengths and time scales that direct numerical simulation (DNS) of the NSE is impossible for the foreseeable future. Consequently, practical engineering calculations are based on some model simplifications of the NSE, with Reynolds stress models being the most popular approach; see, e.g., the book [12]; the review [13], and references therein. The idea of Reynolds (see, e.g., Ref. [14]) was to divide the velocity field into a mean flow part $\mathbf{V}(\mathbf{r})$ and a turbulent fluctuating part $\mathbf{u}(\mathbf{r},t)$ with zero mean and to approximate in some way the hierarchy of equations for various correlation functions (correlators). The equation for $\mathbf{V}(\mathbf{r})$ contains the so-called Reynolds stress term, a second-order correlator of $\mathbf{u}(\mathbf{r},t)$. The right hand side (RHS) of the equation for the Reynolds stress contains five different terms: the rates of production, dissipation, turbulent transport, and viscous diffusion, and the velocity pressure gradient term. These are one-point, second- and third-order correlators of velocity and velocity gradients and the pressure-gradient correlator. The equation for only one such object, the dissipation

rate, already contains eight correlators up to fourth order in the velocity, which are usually modeled by various closure procedures in terms of lower order objects. The simplest, old-fashioned Millionshchikov closure ([14], p. 241) is often invoked. It uses the nonrealistic assumption of Gaussian statistics of turbulence. To improve the situation one can use a set of phenomenological constants, which can be found by comparison of the results of model calculations with the results of DNS or experiments on benchmark flows.

There have been attempts to use more advanced field theoretical approaches developed in the theory of homogeneous turbulence, e.g., the Yakhot-Orszag version of the renormalization group (RNG) approach [15,16]. Instead of going into detailed criticism of this approach, already done in Ref. [17], we just make two general remarks about it, which are also relevant to most attempts at straightforward transfer of the field theoretical methods of fully developed, fine-scale, homogeneous turbulence to the case of wall-bounded flows. First, in most cases (RNG, diagrammatic perturbation approach, etc.) the turbulence is assumed to be excited by some artificial external force with Gaussian statistics. This is a reasonable simplification of the real picture, if one deals with turbulent scales that are deep enough in the inertial interval. However, this is definitely not a realistic assumption for large scales, which are important in the energy and mechanical momentum balance in wall-bounded turbulence. Second, in most cases, the field theoretical approaches to homogeneous turbulence are formulated in the **k** representation or explicitly assuming space homogeneity. In this way one gets the required closure relationships, say between the effective turbulent viscosity ν_T, the density of the kinetic energy $\mathcal{E}$, and the rate of energy dissipation (used in the popular $\overline{K}$-$\overline{\epsilon}$ version of the Reynolds stress model). However, at least two of these objects (ν_T and $\mathcal{E}$) are not locally defined; they are dominated by the largest eddies in the system, usually of scales close to the distance to the wall. Therefore one has to be extremely careful in applying the resulting relations to wall-bounded flows in which the characteristic length of inhomogeneity is exactly the distance to the wall. A price to pay for this simplification is that the phenomenological constants may depend on the flow geometry or even on the position in the flow.

By introducing enough adjustable parameters (sometimes geometry dependent), one can reach the engineering goal of modeling by computer some mean and turbulent characteristics of particular flows of practical importance. However, important aspects of the basic physics of wall-bounded turbulence remain unclear, being masked by numerous details, or even incorrectly reproduced.

The main goal of this paper is to suggest a physically transparent and analytically analyzable model of wall-bounded flows. The model describes the interplay of two main physical phenomena in wall flows: the energy cascade toward small scales (as in developed homogeneous turbulence) and the cascade of the mechanical momentum toward the wall in the physical space. Our model is a generalization of the shell model of homogeneous turbulence to the case of inhomogeneous turbulence and accounts for a nonuniform profile of the mean velocity. Simplifying assumptions are made from the very beginning, at the level of the basic, dynamical equations of motion. These equations involve only two parameters, responsible for the energy and mechanical momentum fluxes. These parameters can be evaluated by DNS of the NSE, but currently they are chosen to reproduce the von Kármán constant κ_K and constant B in the universal logarithmic profile of the mean velocity near a flat plane.

Our model is oriented toward the classical examples of wall turbulence, like channel and pipe flows and planar and circular Couette flows. The physical description of the model and its equations of motion are presented in the following subsection.

B. Brief review of multizone shell model

For dealing with inhomogeneous wall turbulence we suggest in this paper a *piecewise homogeneity approximation* in which the cross-sectional area of the flow, S, is subdivided into a set of j *zones*. The area of the first zone, responsible for the core of the flow, $S_1 \approx S/2$, and the areas of the next j zones, S_j, decrease toward the wall as $S_j \propto 2^{-j}$. In each j zone, the statistics of turbulence is assumed to be space homogeneous and is described by its own shell model

$$\frac{du_{nj}(t)}{dt} = -\nu_n \kappa_n^2 u_{nj} + \mathcal{N}_{nj} + \Delta_{nj} w_n \tag{1.1}$$

for the shell velocities $u_{nj}(t)$, which are responsible for turbulent fluctuations of the (dimensionless) scale $s_n \sim 2^{-n}$, referred to below as (nj) *eddies*. Hereafter, Δ_{nj} is the Kronecker symbol (1 for $n=j$ and 0 otherwise). Equation (1.1) accounts for the viscous damping term with some effective viscosity $\nu_n \sim \nu_0$, where ν_0 is the kinematic viscosity of the fluid. The effective shell wave vector $\kappa_n \propto 1/s_n$. The nonlinear term in Eq. (1.1), $\mathcal{N}_{nj}$, is given by Eq. (2.16) and describes the usual triad interaction of nearest shells, inside a given j zone, Eq. (2.12), and some interzone interaction term of similar type. The production term w_n is responsible for the energy flux from the mean flow to the turbulent subsystem and is given below by Eq. (3.23).

Our goal is to describe the mean velocity profile $\langle \mathbf{V}(\boldsymbol{\rho},t)\rangle$, in which $\boldsymbol{\rho}$ is the two-dimensional radius vector in the cross section of the flow, $\boldsymbol{\rho} \perp \hat{\mathbf{x}}$, where $\hat{\mathbf{x}}$ is the streamwise direction. To this end we introduce additional variables $V_j(t)$ with a prescribed space dependence $\mathbf{\Phi}_j(\boldsymbol{\rho})$, uniquely determined by the flow geometry. The variables $V_j(t)$ can be understood as complex amplitudes of the near-wall coherent structures of the dimensionless scale s_j, which is the same as the scale of the (nj) eddies: $s_j = h_n$ for $n=j$. The functions $\mathbf{\Phi}_j(\boldsymbol{\rho})$ are chosen such that $\mathbf{\Phi}_{j+1}(\boldsymbol{\rho}) \simeq \mathbf{\Phi}_j(2\boldsymbol{\rho})$ and they form an orthonormal (but incomplete) basis. We call it the *PM basis*, because (in spite of its incompleteness) it is chosen such as to represent *exactly* the densities of the mechanical linear and angular momenta $\mathcal{P}$ and $\mathcal{M}$ in terms of $V_j(t)$ only:

$$\mathcal{P} = \sum_j s_j \,\mathrm{Re}[V_j(t)], \quad \mathcal{M} = \sum_j s_j R_j \,\mathrm{Im}[V_j(t)]. \tag{1.2}$$

Here R_j is the characteristic distance of the j zone from the centerline of the flow. The *PM* basis also allows one to reconstruct the spatial dependence of the mean flow (and its time dependent fluctuations) with finite (but very good) accuracy,

$$\mathbf{V}(\boldsymbol{\rho},t)\approx\mathbf{V}_{PM}(\boldsymbol{\rho},gt)\equiv\mathrm{Re}\left[\sum_j V_j(t)\boldsymbol{\Phi}_j(\boldsymbol{\rho})\right]. \quad (1.3)$$

For the *PM velocities* $V_j(t)$ we suggest a simple *momentum equation*

$$\frac{dV_j(t)}{dt}=-\nu_j\kappa_j^2V_j+\nabla p+W_j, \quad (1.4)$$

which includes the viscous term $\nu_j\kappa_j^2V_j$, pressure gradient $\nabla p>0$, and Reynolds stress term W_j, which accounts for the exchange of the mechanical momentum between nearest zones in the flow and is given by Eq. (3.15d).

It is crucially important that the suggested *multi zone shell model*, Eqs. (1.1) and (1.4), preserves (in the unforced, inviscid limit) all the integrals of motion relevant in the problem: the energy $\mathcal{E}$ and mechanical momenta $\mathcal{P}$ and $\mathcal{M}$; and that it respects Galilean and ''asymptotic'' scale invariance together with the NSE type of nonlinearity. The model in a relatively simple and analytically transparent manner describes the basic physical phenomena in wall-bounded flows for a huge interval of Reynolds numbers. The model allows one to study the interplay of temporal intermittency in the cascades and spatial momentum transfer, which may be important, for example, in the problem of drag reduction in wall-bounded flows.

C. The plan of the paper

Section II is devoted to the statistical description of the turbulent part of the multizone shell (MZS) model Eq. (1.1). First, in Sec. II A we describe a way from the NSE to a standard shell model of homogeneous turbulence that allows generalization for space inhomogeneous turbulence. Next, in Sec. II B we formulate a piecewise homogeneity approximation: the cross-sectional area of the flow, S, is subdivided into a set of j zones, in each of which the statistics of turbulence is assumed to be space homogeneous. This allows us to use the standard shell model for every j zone and to describe the turbulence in the whole flow by the set of shell velocities $u_{nj}(t)$ for turbulent fluctuations of the scale proportional to $1/2^n$.

In Sec. III we derive the dynamical equation of motion for the so-called *PM* velocities V_j, which allows one to reconstruct with good accuracy the mean velocity profile $\mathbf{V}(\boldsymbol{\rho})$ in the cross section of the flow. In particular, in Sec. III B we introduce the *PM* basis for a wide class of wall-bounded flows, which connects $\mathbf{V}(\boldsymbol{\rho})$ and V_j. In Sec. III C we derive Eq. (1.4) for V_j and for all terms involved in Eq. (1.4).

We start Sec. IV with a summary of the resulting MZS equations, presenting them, in Sec. IV A, in dimensionless form (4.3), convenient for further analysis. In particular, we discuss the conservation laws (Sec. IV B) and the symmetries (Secs. IV C and IV D) of the MZS model. In Sec. IV D we derive a version of the MZS model for the turbulent boundary layer near a flat plane, Eqs. (4.19).

Section V presents a detailed analytical study of the MZS equations in a set of approximations realistic at various values of *Re*. In Sec. V A we show that the MZS model describes the stable laminar velocity profile for small Re and its instability at some threshold value of $Re=Re_{\mathrm{cr}}$. Next, in Sec. V B we study the MZS model in the approximation of near-wall eddies, neglecting the turbulent energy cascade. This effect is accounted for in Sec. V C in the approximation of turbulent viscosity. Section V D is devoted to a numerical analysis of the MZS model.

In Sec. VI, we summarize our findings and suggest a possible generalization of the model for the description of turbulent flows laden with long-chain polymeric additives (in connection with the problem of drag reduction) or with heavy microparticles, etc.

D. Notation and definitions

For the reader's convenience we collect in this subsection some frequently used notation and important definitions.

$\hat{\mathbf{x}}$ and $\boldsymbol{\rho}$ are the streamwise direction and the two-dimensional radius vector in the cross section of a flow, $\boldsymbol{\rho}\perp\hat{\mathbf{x}}$. In a channel $\boldsymbol{\rho}=(y,z)$, with y as the wall normal and z as the spanwise directions.

$S_\perp$, $P_\perp$, and L are the cross-sectional area, the perimeter, and the characteristic length of a cross section:

$$S_\perp=\int d\boldsymbol{\rho}, \quad L\equiv S_\perp/P_\perp. \quad (1.5)$$

In a channel of width $2H$, $L=H$; in a pipe of radius R, $L=R/2$.

∇p is the external pressure gradient, which is a positive constant:

$$\nabla p\equiv-\frac{dp(x)}{dx}>0. \quad (1.6)$$

τ and U_τ are the characteristic time and the velocity in the flow:

$$\tau\equiv\sqrt{L/\nabla p}, \quad U_\tau\equiv\sqrt{L\nabla p}. \quad (1.7)$$

The wall shear stress is U_τ^2.

ν_0 and *Re* are the kinematic viscosity and the friction Reynolds number

$$Re\equiv U_\tau L/\nu_0. \quad (1.8)$$

f' and f'' are the real and imaginary parts of some complex object f (constant, variable, function, etc.):

$$f'\equiv\mathrm{Re}[f], \quad f''\equiv\mathrm{Im}[f]. \quad (1.9)$$

n, j, and p are dummy indices (natural numbers), reserved for the scale (or shell), zone, and position indices; some objects can be related to both the shells and zones. They are used with both n and j indices.

s_j and σ_j are the fraction of the cross-sectional area occupied by the j zone, and the fraction of the cross-sectional area occupied by all zones toward the wall, starting from the zone j:

$$s_j \equiv \frac{S_j}{S_\perp}, \quad \sigma_j \equiv \sum_{i=j}^{\infty} s_i, \quad \sigma_1 = \sum_{j=1}^{\infty} s_j = 1. \tag{1.10}$$

L_j ($\equiv s_j L$) is the width of the j zone and L_n the characteristic scale in the n shell.

κ_n [$\equiv 1/(2L_n)$] is the wave number in the n shell; κ_j is the wave number of the j zone.

$\mathcal{E}$, $\mathcal{P}$, and $\mathcal{M}$ are the densities of the energy and of the mechanical linear and angular momenta ($\hat{\mathbf{x}}$ projections).

$\varepsilon^{\pm}$, $\mathfrak{p}^{\pm}$, and $\mathfrak{m}^{\pm}$ are the total rates of pumping (with $+$) and dissipation (with $-$) of the conserved quantities $\mathcal{E}$, $\mathcal{P}$, and $\mathcal{M}$.

$\varepsilon_j^{\pm}$, $\mathfrak{p}_j^{\pm}$, and $\mathfrak{m}_j^{\pm}$ are the rates of pumping (with $+$) and dissipation (with $-$) in the j zone (of $\mathcal{E}$, $\mathcal{P}$, and $\mathcal{M}$).

ε_j, $\mathfrak{p}_j$, and $\mathfrak{m}_j$ are the fluxes of $\mathcal{E}$, $\mathcal{P}$, and $\mathcal{M}$ from the j to the $(j+1)$ zone.

The scalar product of complex vector functions $\mathbf{A}(\boldsymbol{\rho})$ and $\mathbf{B}(\boldsymbol{\rho})$ is

$$(\mathbf{A},\mathbf{B}) \equiv \int \mathbf{A}^*(\boldsymbol{\rho}) \cdot \mathbf{B}(\boldsymbol{\rho}) \frac{d\boldsymbol{\rho}}{S_\perp}. \tag{1.11}$$

$\phi_m^+(\boldsymbol{\rho})$ and $\phi_m^-(\boldsymbol{\rho})$ are the even and odd eigenfunctions of the two-dimensional Laplace operator in the cross section of the flow with no-slip boundary conditions, $\phi_m^{\pm}(-\boldsymbol{\rho}) = \pm\phi^{\pm}(\boldsymbol{\rho})$.

$\mathbf{\Phi}_j(\boldsymbol{\rho}) = \mathbf{\Phi}_j'(\boldsymbol{\rho}) + i\mathbf{\Phi}_j''(\boldsymbol{\rho})$ are *PM* basis functions, Eq. (A2).

$V_{PM}(\boldsymbol{\rho})$ and V_j are the *PM* velocity in the coordinate and j representations, related by Eq. (3.3).

u_{nj} is the velocity of turbulent fluctuation of the scale proportional to 2^{-n} in the j zone [(nj) eddies]; $u_j \equiv u_{jj}$.

II. STATISTICAL MULTIZONE SHELL MODEL FOR TURBULENT FLUCTUATIONS

A. From the NSE to shell models of homogeneous turbulence

In this subsection we present a rederivation of the standard shell model of space homogeneous turbulence in a way that allows us to generalize it in Sec. II B for the case of space inhomogeneity.

1. "Cell basis," wavelets, and "$(n\mathbf{p})$ eddies"

Consider for simplicity an incompressible turbulent velocity $\mathbf{u}(\mathbf{r},t)$ in a periodic box of size $L\times L\times L$. Instead of the $\mathbf{r}$ or $\mathbf{k}$ representation, we introduce here a "*cell basis*" $\mathbf{\Psi}_{n\mathbf{p}}(\mathbf{r})$, which is quite similar to wavelet bases (for an easy-to-read, introductory text about the theory of wavelets, see, e.g., [18]). Similar to the wavelet bases, the cell bases reflect both spatial scales of turbulent structures (as in the $\mathbf{k}$ representation) and their position in the physical space (as in the $\mathbf{r}$ representation) but account for the actual boundary conditions of the flow. *The cell index* $(n,\mathbf{p})$ consists of the scale index $n=1,2,\ldots,\infty$ and the position index $\mathbf{p}=(p_x,p_y,p_z)$.

The *scale index* $n=1,2,\ldots,\infty$ defines the characteristic width L_n (in all directions) of the function $\mathbf{\Psi}_{n\mathbf{p}}(\mathbf{r})$, which some $(n\mathbf{p})$ cell of size $L_n = L/2^n$ "occupies" in space.

The *position index* $\mathbf{p}=(p_x,p_y,p_z)$ defines the position $\mathbf{R}_{n\mathbf{p}}$ of the $(n\mathbf{p})$ cell:

$$\mathbf{R}_{n\mathbf{p}} \equiv \mathbf{p}L_n, \quad \mathbf{p}=(p_x,p_y,p_z),$$

$$\mathbf{p}\in\mathcal{C}_n \Leftrightarrow p_\alpha = 1,2,\ldots,2^n, \quad \alpha = x,y,z. \tag{2.1}$$

One can imagine that, for any given n, the set of $(n\mathbf{p})$ cells with $\mathbf{p}\in\mathcal{C}_n$ fills a periodic L^3 box. The turbulent velocity field $\mathbf{u}(\mathbf{r},t)$ is given by

$$\mathbf{u}(\mathbf{r},t) = \sum_{n=1}^{\infty} \sum_{\mathbf{p}\in\mathcal{C}_n} \mathrm{Re}[U_{n\mathbf{p}}(t)\mathbf{\Psi}_{n\mathbf{p}}(\mathbf{r})], \tag{2.2}$$

where the amplitude of the cell expansion, $U_{n\mathbf{p}}(t)$, is the velocity difference across the separation L_n in the $(n\mathbf{p})$ cell.

It is convenient to normalize the cell basis as follows:

$$\int_0^L\int_0^L\int_0^L \mathbf{\Psi}^*_{n\mathbf{p}}(\mathbf{r})\cdot\mathbf{\Psi}_{n'\mathbf{p}'}(\mathbf{r})\frac{dx\,dy\,dz}{L^3} = 2v_n\Delta_{nn'}\Delta_{\mathbf{pp}'},$$

$$\int_0^L\int_0^L\int_0^L \mathbf{\Psi}_{n\mathbf{p}}(\mathbf{r})\cdot\mathbf{\Psi}_{n'\mathbf{p}'}(\mathbf{r})\frac{dx\,dy\,dz}{L^3} = 0. \tag{2.3a}$$

Here $v_n = 2^{-3n}$ is the dimensionless part of the total volume per one mode in the nth cell.

Equations (2.2) and (2.3) give the Parseval identity for the density of the turbulent energy in the form

$$\mathcal{E} \equiv \int_0^L\int_0^L\int_0^L \frac{|u(\mathbf{r},t)|^2}{2}\frac{dx\,dy\,dz}{L^3} = \sum_{n=1}^{\infty}\mathcal{E}_n(t), \tag{2.4a}$$

$$\mathcal{E}_n(t) = v_n \sum_{\mathbf{p}\in\mathcal{C}_n} \frac{|U_{n\mathbf{p}}(t)|^2}{2}. \tag{2.4b}$$

This equation supports our interpretation of $U_{n\mathbf{p}}(t)$ as the velocity difference across the separation L_n in the $(n\mathbf{p})$ cell. We will refer to these fluctuations as the $(n\mathbf{p})$ eddy.

A particular choice of the cell functions $\mathbf{\Psi}_{n\mathbf{p}}(\mathbf{r})$ is not important for us here. Notice only that for large n the basic cell functions become scale invariant and may be obtained by dilatations of one (or a few) n independent function $\mathbf{\Psi}_\infty(x)$. In this limit the cell basis becomes the wavelet one with $\mathbf{\Psi}_\infty(x)$ as the so-called $\mathcal{R}$ wavelet [18]. An explicit example of a divergence-free three-dimensional vector $\mathcal{R}$ wavelet function and is given in [6].

The cell functions $\mathbf{\Psi}_{n\mathbf{p}}(\mathbf{r})$ form a complete orthonormal basis, and therefore one can derive the *exact equation of motion* for $U_{n\mathbf{p}}(t)$ by the Galerkin projection of the NSE:

$$\frac{dU^{\sigma}_{n\mathbf{p}}(t)}{dt} = -\sum_{\mathbf{p}'} \Gamma_{n,\mathbf{p}\mathbf{p}'} U^{\sigma}_{n\mathbf{p}'}(t) + \sum_{n'n''} \sum_{\mathbf{p}'\mathbf{p}''} \sum_{\sigma'\sigma''=\pm} T^{\sigma\sigma'\sigma''}_{nn'n'',\mathbf{p}\mathbf{p}'\mathbf{p}''} U^{\sigma'}_{n'\mathbf{p}'}(t) U^{\sigma''}_{n''\mathbf{p}''}(t), \tag{2.5}$$

where $\sigma, \sigma', \sigma'' = \pm$ are sign indices, and we accept the convention $U^{-}_{n\mathbf{p}} \equiv U_{n\mathbf{p}}$ and $U^{+}_{n\mathbf{p}} \equiv U^{*}_{n\mathbf{p}}$. The explicit forms of the damping parameters Γ and amplitudes T depend on the basis; see, e.g., [6].

2. Basic assumptions of the standard shell models

Consider briefly the physical simplifications that allow one to reduce the NSE to the shell model of homogeneous turbulence. Unlike the similar discussion in [6], we emphasized the assumption of space homogeneity and the possibility of relaxing this assumption in order to generalize shell models for the space inhomogeneous case.

The standard shell models of homogeneous turbulence follow from the exact Eq. (2.5) with the following simplifying assumption of a statistical nature:

$$U_{n\mathbf{p}}(t) \Rightarrow u_n(t) A_{n\mathbf{p}}, \tag{2.6a}$$

$$\overline{A_{n\mathbf{p}}} = 0, \quad \overline{|A_{n\mathbf{p}}|^2} = 1. \tag{2.6b}$$

Here $A_{n\mathbf{p}}$ are time independent, random amplitudes, and the overbar denotes averaging over yet unknown statistics of $A_{n\mathbf{p}}$, which is generated by the NSE (2.5). The dynamical content of $u_n(t)$ is the "typical" (in the statistical sense) time dependence of all $(n\mathbf{p})$ eddies; in particular, $\langle |u_n|^q \rangle$ is supposed to have the same scaling exponents as the q-order velocity structure functions in NSE turbulence; see, e.g., [5].

The physical arguments behind Eq. (2.6) may be based on the fact that in homogeneous turbulence all velocities $U_{n\mathbf{p}}(t)$ with different $\mathbf{p}$ have the same statistics. Equation (2.6) therefore neglects only the difference between the actual time realizations of $n\mathbf{p}$ velocities $U_{n\mathbf{p}}(t)$ of the same scale (the same scale index n), but occupying different cells (different position index $\mathbf{p}$). The ensemble of the time realizations is replaced by the time independent ensemble of $A_{n\mathbf{p}}$. With the assumption (2.6), Eq. (2.5) yields

$$\frac{du_n(t)}{dt} = -\gamma_n u_n(t) + N_n, \tag{2.7a}$$

$$\gamma_n = \sum_{\mathbf{p}'} \Gamma_{n,\mathbf{p}\mathbf{p}'} \overline{A_{n\mathbf{p}} A_{n\mathbf{p}'}}, \tag{2.7b}$$

$$N_n = \sum_{n'n'',\sigma'\sigma''} S^{\sigma'\sigma''}_{nn'n''} u^{\sigma'}_{n'}(t) u^{\sigma''}_{n''}(t), \tag{2.7c}$$

$$S^{\sigma'\sigma''}_{nn'n''} = \sum_{\mathbf{p}'\mathbf{p}''} T^{\sigma'\sigma''}_{nn'n'',\mathbf{p}\mathbf{p}'\mathbf{p}''} \overline{A_{n\mathbf{p}} A_{n'\mathbf{p}'} A_{n''\mathbf{p}''}}. \tag{2.7d}$$

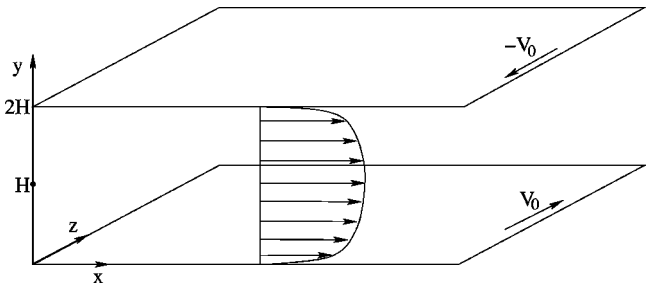

FIG. 1. Geometry of the channel and the plane Couette flow between two parallel planes separated by $2H$ in the cross-stream direction y. In the simple channel flow the pressure gradient is applied in the "streamwise" direction x and the mean velocity $\overline{V}(y)$ is oriented also along x. In the plane Couette flow the lower wall $(y=0)$ is moving in z (span-wise) direction with some velocity V_0, while the upper wall $(y=2H)$ is moving in the opposite direction. In this case $\overline{V}(y)$ has z-projection. For both flows (and their hybridization) the three-dimensional velocity fluctuations are space-homogeneous in the $x-z$ plane.

The correlation functions of $A_{n\mathbf{p}}$ can be evaluated with some reasonable statistical assumptions (for instance, with some closure procedure, like the direct interaction approximation; see, e.g., [6]).

Under assumption (2.6), Eq. (2.4b) gives the usual equation for the density of the total energy of the nth scale: $\mathcal{E}_n(t) = 1/2|u_n(t)|^2$. Different shell models correspond to various further simplifications of the nonlinear term (2.7c). For example, in the Sabra shell model [3],

$$N_n = i[a\kappa_{n+1} u^{*}_{n+1} u_{n+2} + b\kappa_n u^{*}_{n-1} u_{n+1} - c\kappa_{n-1} u_{n-2} u_{n-1}], \tag{2.8a}$$

$$\kappa_n \propto 2^n, \quad a+b+c=0. \tag{2.8b}$$

Notice that the scale index n in Eqs. (2.7) and (2.8) for shell models becomes the *shell index*.

B. Piecewise homogeneity approximation and multizone shell model for turbulent fluctuations

The turbulent fluctuations in wall-bounded flows are not space homogeneous due to the spatial dependence of the mean velocity profile, which, in its turn, is also affected by the turbulent fluctuations. Due to the inhomogeneity of turbulence, the shell model approach discussed in Sec. II A has to be revised, which is the subject of this subsection. For concreteness we discuss the planar geometry of channel flow of width $2H$ in the cross-stream direction y (see Fig. 1). In further analysis we consider only the lower half of the channel, $0<y<H$, having in mind that the flow in the second half of the channel, $H<y<2H$, is statistically identical to that in the first one.

Clearly, the core of the flow (say, for $H/2<y<H$) may be approximately viewed as homogeneous. Let us call this region the 1 zone. The next region $H/4<y<H/2$, in which the mean velocity profile $V(y)$ begins to decrease towards the wall, we call the 2 zone. Notice that the width of the 2 zone, $H_2 = H/4$, is one-half of the 1-zone width, $H_1 = H/2$. There-

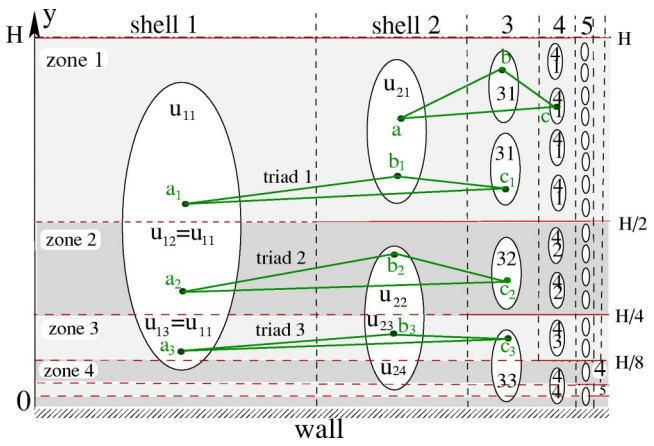

FIG. 2. Zones, shells, and triad interactions in the multizone shell model for the channel geometry. Regions of localization of $(n\mathbf{p})$ eddies are shown schematically as ellipses with corresponding numbers inside. The near-wall eddies have $n=j$. They also occupy all j zones toward the wall, with $j>n$.

fore, with approximately the same accuracy we can consider the statistics of turbulence in the 2 zone as homogeneous, but different from that in the 1 zone.

Similarly, one expects that the mean velocity difference across each succeeding j zone of width $H_j=H/2^j$ will be more or less the same. This is the motivation to define the j zone in a scale invariant manner, as $2^{-j}H<y<2^{-(j-1)}H$ and to approximate the turbulence inside each such zone as homogeneous.

The approximation of the piecewise homogeneity allows one to use the shell-model reduction, Eq. (2.6), inside each j zone, similarly to that in the whole space for homogeneous turbulence:

$$U_{n\mathbf{p}}(t)\Rightarrow u_{nj}(t)A_{n\mathbf{p}_j},\quad 1\leqslant j\leqslant n, \tag{2.9a}$$

$$\overline{A_{n\mathbf{p}}}=0,\quad \overline{|A_{n\mathbf{p}}|^2}=1,$$

$$u_{nj}=u_{nn},\quad j>n. \tag{2.9b}$$

Here $\mathbf{p}_j$ belong to the j zone, in the sense that the $(n\mathbf{p}_j)$ cells are inside the j zone. We introduced in Eq. (2.9a) the velocity of (nj) eddies, in the nth shell in the j zone. Equation (2.9b) reflects the fact that the near-wall (nj) eddies with zone index $j>n$ belong simultaneously to the j zone with $j=n$ (see Fig. 2). Therefore in our model all $u_{nj}(t)$ with $j>n$ are just $u_{nn}(t)$.

With Eqs. (2.9) one gets from Eqs. (2.4b)

$$\mathcal{E}_n(t)=\sum_{j=1}^{\infty}\frac{H_j}{H}\mathcal{E}_{nj}(t),\quad \mathcal{E}_{nj}(t)=\frac{|u_{nj}(t)|^2}{2}, \tag{2.10}$$

where $\mathcal{E}_{nj}$ is the energy density of the nth shell in the j zone of width $H_j=H/2^j$.

Using Eqs. (2.9) and (2.5), one gets the equation of motion of the multizone shell model for turbulent fluctuations:

$$\frac{du_{nj}(t)}{dt}=-\gamma_n u_{nj}(t)+\mathcal{N}_{nj}+\Delta_{nj}w_j, \tag{2.11}$$

in which we have added by hand the production term w_j, describing the energy pumping to the turbulent system. This term will be clarified in the following section by Eq. (3.23).

The nonlinear term $\mathcal{N}_{nj}$ in Eq. (2.11) describes the total energy balance for the nth shell in the j zone. There are two distinct geometries: $j<n$ and $j\geqslant n$. In the latter case it is enough to describe the energy balance for $j=n$, since all $u_{nj}=u_{nn}$ for $j>n$.

All eddies with $j<n$ are fully placed in the same zone (e.g., the eddies of shells $n=2$, 3, and 4, which belong to the first zone; see Fig. 2). Therefore in this case we can use for $\mathcal{N}_{nj}(t)$ a standard shell model expression for N_n, in which $u_{nj}\Rightarrow u_n$. In this paper we adopt the Sabra version of the N_{nj} term, generalizing Eq. (2.8):

$$\mathcal{N}_{nj}(t)=N_{nj}(t)\quad \text{for } j<n, \tag{2.12a}$$

$$N_{nj}=i[a\kappa_{n+1}u^*_{n+1,j}u_{n+2,j}+b\kappa_n u^*_{n-1,j}u_{n+1,j}-c\kappa_{n-1}u_{n-2,j}u_{n-1,j}]. \tag{2.12b}$$

The energy balance of the near-wall eddies $(n=j)$ is quite different. As one sees in Fig. 2 (on the example of the eddy in the first shell), the near-wall eddies participate in triad interactions of three types. *Triad 1* involves one near-wall eddy and two bulk eddies [the $(u_{11}$-u_{21}-$u_{31})$ triad of the first zone in the above example]. For this interaction we will use Eq. (2.8) but with different parameters: a_1, b_1, and c_1. *Triad 2* involves two near-wall eddies and one bulk eddy [the $(u_{12}$-u_{22}-$u_{32})$ triad of the second zone in Fig. 2]. Here we will use Eq. (2.8) with the parameters a_2, b_2, and c_2. *Triad 3* involves three near-wall eddies [the $(u_{13}$-u_{23}-$u_{33})$ triad of the third zone in the above example]. Here we will again use Eq. (2.8) with the parameters a_3, b_3, and c_3.

The relationships between the four set of interaction parameters [(a,b,c) and (a_p,b_p,c_p), $p=1,2,3$] may be found from (i) the requirement of the conservation of energy and (ii) the "correspondence principle:" For the space homogeneous case (u_{nj} is independent of the zone index j) the multizone model must coincide with the usual shell model for homogeneous turbulence (in our case, with the Sabra model).

The above two requirements give

$$a_1=a/2,\quad a_2=a_3=a/4,$$

$$b_1=b,\quad b_2=b_3=b/2,$$

$$c=c_1=c_2=c_3. \tag{2.13}$$

These equations may be interpreted as follows. In the triads 1 only one-half of the largest eddy belongs to the same zone as two smaller ones. This gives $a_1=a/2$. Two smaller eddies in triad 1 fully belong to their zone. This corresponds to $b_1=b$ and $c_1=c$. In the triads 2 only one-quarter of the largest eddy belongs to the same zone as two smaller ones. Therefore $a_2=a/4$. In this triad only one-half of the middle eddy belongs to the same zone as the smallest one. This

corresponds to $b_2=b/2$. The smallest eddy in the triad belongs fully to its own zone, and we take $c_2=c$. In triads 3 only one-quarter of the largest eddy, one-half of the middle one, and the full smallest eddy belong to the same set of zones (zones 3,4, etc., in our example). This corresponds to the relationships $a_3=a/4$, $b_3=b/2$, and $c_3=c$.

The total contribution of the three types of triad interaction to the nonlinearity of the near-wall eddies can be summarized as follows:

$$\mathcal{N}_{nn}=\frac{1}{4}[2N_{n,n}+N_{n,n+1}+N_{n,n+2}]. \tag{2.14}$$

One can join the two equations (2.12) and (2.14) and write

$$\mathcal{N}_{nj}=N_{nj}+\Delta_{nj}\left[\frac{1}{4}(N_{n,n+1}-N_{nn})+\frac{1}{4}(N_{n,n+2}-N_{nn})\right]. \tag{2.15}$$

Obviously, in the homogeneous case the second term in the RHS of Eq. (2.15) vanishes and one recovers the usual shell model for homogeneous turbulence with $\mathcal{N}_{nj}\Rightarrow N_n$.

Notice that the explicit form of this equation reflects the fact that we have accounted only for the triad interactions involving the nearest shells $(n-1,\ n,$ and $n+1)$ and the particular form of the channel subdivision in the zones $H_j=2^{-j}H$. This subdivision of the cross-sectional area on zones is reasonable for the scale invariant case of a turbulent boundary layer near a flat plane. The physically motivated subdivision in particular flow geometries will be discussed in the following section. In the general case Eq. (2.14) is changed as follows:

$$\mathcal{N}_{nj}=N_{nj}+\Delta_{nj}\sum_{i=n+1}^{\infty}\frac{s_i}{\sigma_j}(N_{ni}-N_{nn}),$$

$$\sigma_j\equiv\sum_{i=j}^{\infty}s_i, \tag{2.16}$$

with an arbitrary dependence of the (dimensionless) j zone areas s_j on j and an arbitrary form of the nonlinear term N_{nj}. The fact that under the sum one has the difference $(N_{nj}-N_{nn})$ guarantees the correspondence principle, while the weights s_i/σ_j follow from the requirement of conservation of the total energy, which in the case of an arbitrary zone division is given by a natural generalization of Eq. (2.10) with H_j/H replaced by s_j:

$$\mathcal{E}_n(t)=\sum_{j=1}^{\infty}s_j\mathcal{E}_{nj}(t),\quad \mathcal{E}_{nj}(t)=\frac{|u_{nj}(t)|^2}{2}. \tag{2.17}$$

III. DYNAMICAL MULTISCALE MODEL FOR THE *PM* VELOCITY

A. Mechanical momenta *P* and *M* and statistics versus dynamics dilemma

Unbounded turbulence may be described in a reference system with a zero mean velocity. In that system the total linear momentum vanishes: $\mathbf{P}=\mathbf{0}$. Due to Galilean invariance the space homogeneous velocity does not interact with the turbulent fluctuations. Therefore one can consider turbulence in any other reference system with $\mathbf{P}\neq\mathbf{0}$ with the same result for the statistics of turbulence. Hence, the mechanical momentum is not a relevant integral of motion for unbounded turbulence. This is not the case for wall-bounded turbulence, in which the Galilean invariance is broken by the presence of the walls. The conservation laws for the total linear momentum $\mathbf{P}$ (as well as for the total angular momentum $\mathbf{M}$) give an important constraint on the expected behavior of the system. For example, in channel and pipe flows, the total input of linear momentum due to the pressure gradient, acting in the whole cross-sectional area of the flow, must be equal to the dissipation of momentum at the walls due to viscous friction. Clearly, an analytical description of wall-bounded turbulence must respect the conservation of $\mathbf{P}$ and $\mathbf{M}$ (in the unforced, inviscid limit).

Consider the mean velocity field $\mathbf{V}(\boldsymbol{\rho})$ in simple flows with translational symmetry in the streamwise direction $\hat{\mathbf{x}}\|\mathbf{P}$, in which also $\mathbf{M}\|\hat{\mathbf{x}}$. Here $\boldsymbol{\rho}$ is the radius vector in the cross section of the flow, $\boldsymbol{\rho}\perp\hat{\mathbf{x}}$. Examples of such flows are channel and pipe flows, planar Couette flow (Fig. 1), circular Couette flow, etc. Instead of $\mathbf{P}$ and $\mathbf{M}$, it is more convenient to deal with their volume densities $\mathcal{P}$ and $\mathcal{M}$, defined as follows:

$$\mathcal{P}=\mathcal{P}_x=(\hat{\mathbf{x}},\mathbf{V}), \tag{3.1a}$$

$$\mathcal{M}=\mathcal{M}_x=(\boldsymbol{\mathcal{R}},\mathbf{V}),\quad \boldsymbol{\mathcal{R}}\equiv\hat{\mathbf{x}}\times\boldsymbol{\rho} \tag{3.1b}$$

where $(\mathbf{A},\mathbf{B})$ is the scalar product (1.11).

Our idea is to divide the full velocity field $\mathbf{V}(\boldsymbol{\rho})$ into two parts, denoted as $\mathbf{V}_{PM}(\boldsymbol{\rho})$ and $\mathbf{V}_T(\boldsymbol{\rho})$, such that the turbulent part $\mathbf{V}_T(\boldsymbol{\rho})$ does not contribute to $\mathcal{P}$ and $\mathcal{M}$:

$$(\hat{\mathbf{x}},\mathbf{V}_T)=0,\quad (\boldsymbol{\mathcal{R}},\mathbf{V}_T)=0, \tag{3.2}$$

and to take special care only with $\mathbf{V}_{PM}(\boldsymbol{\rho})$, contributing to $\mathcal{P}$ and $\mathcal{M}$. This division may be done in many ways; our particular choice will be clarified below by Eq. (3.3).

The description of $\mathbf{V}_{PM}(\boldsymbol{\rho},t)$ may be statistical or dynamical. The statistical description is the straightforward cell-expansion approach to shell models, based on the NSE for $\mathbf{V}_{PM}(\boldsymbol{\rho},t)$ in the cell representation, similar to Eq. (2.5). To continue, one has to find some reasonable statistical simplifications, similar to Eq. (2.9). However, since $\mathcal{P}\neq 0$ and/or $\mathcal{M}\neq 0$, now also $\langle\mathbf{V}_{PM}(\boldsymbol{\rho},t)\rangle\neq 0$ and therefore $\overline{A_{n\mathbf{p}}}$ cannot be approximated as zero. This makes it hardly possible to remain on the level of a statistical description and one has to deal with a detailed, dynamical description of the *PM* velocity $\mathbf{V}_{PM}(\boldsymbol{\rho},t)$ in terms of the NSE. This is the subject of the following subsections.

B. *PM* basis, properties, and interpretation

1. Construction of the basis

In the framework of the MZS model, we approximate the mean velocity profile by the *PM* velocity $\mathbf{V}_{PM}(\boldsymbol{\rho},t)$, which can be projected on the *incomplete* complex *PM* basis $\mathbf{\Phi}_j(\boldsymbol{\rho})$:

$$\mathbf{V}_{PM}(\boldsymbol{\rho},t)\equiv \mathrm{Re}\left[\sum_{j=1}^{\infty} V_j(t)\mathbf{\Phi}_j(\boldsymbol{\rho})\right], \tag{3.3}$$

where the expansion coefficients $V_j(t)$ can be understood as *PM* velocities in the zone representation.

In order to reflect the essential physics of the problem in the *PM* representation, we require the following general properties of the basis functions.

(1) The basis functions $\mathbf{\Phi}_j(y)$ are asymptotically (for $j\to\infty$) scale invariant:

$$\mathbf{\Phi}_{j+1}(\boldsymbol{\rho})\approx\mathbf{\Phi}_j(\lambda\boldsymbol{\rho}), \tag{3.4a}$$

with a *scaling parameter* $\lambda>1$. In this paper we adopt a standard value $\lambda=2$.

(2) The basis functions $\mathbf{\Phi}_j(y)$ form an orthogonal set and thus represent independent contributions to the kinetic energy of the flow:

$$(\mathbf{\Phi}_j,\mathbf{\Phi}_{j'})=2s_j\Delta_{jj'}, \tag{3.4b}$$

$$(\mathbf{\Phi}_j^*,\mathbf{\Phi}_{j'})=0. \tag{3.4c}$$

Here s_j are dimensionless *zone areas* that depend on the explicit form of the basis.

(3) In spite of its incompleteness, the *PM* basis *exactly* represents the relevant linear integrals of motion, namely, linear $\mathcal{P}$ and angular $\mathcal{M}$ mechanical momenta, defined by Eqs. (3.1).

(4) In addition to these three crucial properties, we also require that different basic functions $\mathbf{\Phi}_j(\boldsymbol{\rho})$ belong to different subspaces of the Laplace operator. In this case the viscous term in the zone representation will have the simplest possible diagonal form.

In Appendix A we show that the above requirements are sufficient to determine the unique *PM* basis for any given flow geometry, Eq. (A2), and analyze the properties of such bases in detail. Here we list expressions for the conserved quantities of the NS equation in the *PM* basis that are important for the following discussion. The densities of the linear $\mathcal{P}$ and angular $\mathcal{M}$ mechanical momenta of the flow are given *exactly* as

$$\mathcal{P}=\sum_j s_j V_j'(t), \tag{3.5a}$$

$$\mathcal{M}=\sum_j s_j[R_j V_j''(t)]. \tag{3.5b}$$

Here R_j is defined by Eq. (A7), and, with a high accuracy, may be approximated as the distance from the center of the flow to the wall, i.e., $R_j\approx H$ for the channel.

The energy density associated with the *PM* velocity is

$$\mathcal{E}_{PM}=\sum_j s_j\frac{|V_j|^2}{2}. \tag{3.5c}$$

2. PM basis for the channel and pipe flows

The particular form of the *PM* functions is geometry dependent. To get a feeling of the appearance of these functions, we discuss here two important cases, channel and pipe flows, found in Appendix A, Eqs. (A2), (A13), and (A14). These two examples will serve us in the rest of the paper. Some properties of these specific bases are more general, however, and will be used in the derivation and analysis of the momentum equation for $V_j(t)$.

In Fig. 3 we plot $\Phi_{j,x}'(y)$ and $\Phi_{j,z}''(y)$ for the channel as it follows from Eq. (A2) with Eq. (A13). The functions $\Phi_{j,x}'(y)$ are symmetric with respect to the centerline of the channel $y=H$, whereas $\Phi_{j,z}''(y)$ are antisymmetric. For large j, $\Phi_{j,x}'(y)$ and $\Phi_{j,z}''(y)$ coincide in the lower half of the channel $y<H$ and have an opposite sign for $y>H$. As is clear from (c) and (d) in the near-wall ($y\ll H$) region $\Phi_{j,x}'(y)$ and $\Phi_{j,z}''(y)$ already almost coincide for $j=5$.

For channel flow one can find from Eqs. (A2) and (A13) an explicit asymptotic expression for $\Phi_{j,x}'(y)$ and $\Phi_{j,z}''(y)$ in the limit $j\to\infty$ (actually, $j>4$). For $y<H$,

$$\Phi_{j,x}'(y)\simeq\Phi_{j,z}''(y)\simeq\Phi_{\mathrm{un}}(2^j\pi^2 y/2H), \tag{3.6a}$$

$$\Phi_{\mathrm{un}}(\xi)\equiv\frac{2}{\pi}\left[\mathrm{Si}\left(\frac{2\xi}{\pi}\right)-\mathrm{Si}\left(\frac{\xi}{\pi}\right)\right], \tag{3.6b}$$

where $\mathrm{Si}(x)$ is the sine integral function.

It is expected that the asymptotic form of the basic functions Φ_{un} is the same for any flow geometry, if one expresses them as functions of the distance from the wall. For example, in the pipe one obtains Eq. (3.6a), where y is the distance from the wall, $y=R-\rho$, and H is the radius of the pipe, $H=R$. In Fig. 4 we show the collapse of the rescaled functions $\Phi_j(2H\xi/\pi^2 2^j)$ for $j=5,\ldots,8$ with the universal function $\Phi_{\mathrm{un}}(\xi)$ for the channel (a) and pipe [(b), $H=R$] flows.

3. Geometry of the j zones in the channel and pipe flows

a. Characteristic length of a flow. The cross section of the flow can be characterized by two global parameters, the cross-sectioned area $S_\perp$ and the length of its perimeter $P_\perp$. One can organize from these two objects many combinations with the dimensions of length, $L(\beta)\equiv P_\perp(S_\perp/P_\perp^2)^\beta$, with arbitrary β. For discussion of turbulent flows under an external pressure gradient, the particular choice $\beta=1$,

$$L\equiv L(1)=S_\perp/P_\perp, \tag{3.7}$$

is physically important. The reason is that the total external accelerating force, applied on a unit length of the fluid (in the streamwise direction), is proportional to $S_\perp$:

$$F_{\mathrm{ac}}=\nabla p S_\perp,$$

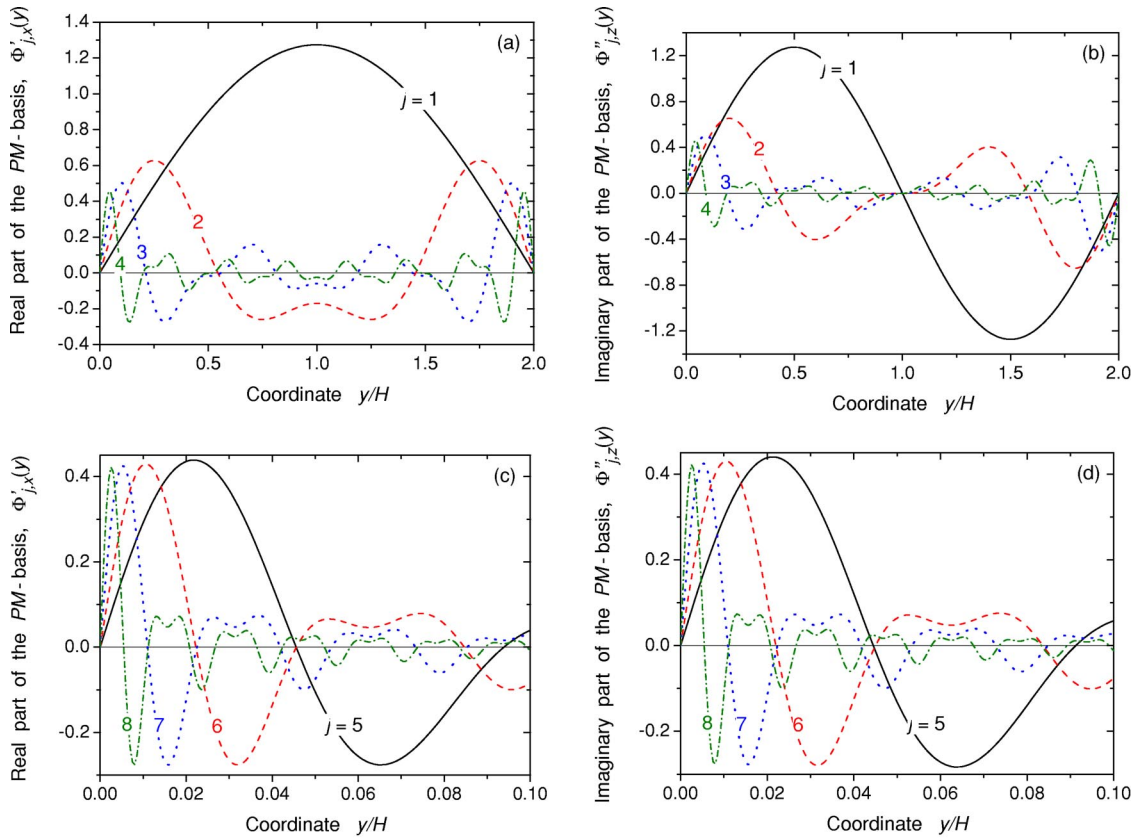

FIG. 3. First functions $\mathbf{\Phi}_j(\xi H)$ describing the mean flow with nonzero mechanical momenta in a channel of width $2H$. In the whole channel $0<\xi<2$. (a) and (b) The *PM* functions $\Phi'_{j,x}(\xi H)$ (a) and $\Phi''_{j,z}(\xi H)$ (b) with $j=1,2,3,4$ for the whole channel. (c) and (d) The *PM* functions with $j=5,6,7,8$ in the near-wall region. (c) $\Phi'_{j,x}(\xi H)$. (d) $\Phi''_{j,z}(\xi H)$.

while the total friction force is proportional to $P_\perp$ (under the simplifying assumption of homogeneity along the perimeter):

$$F_{\text{fric}} = \nu_0 P_\perp \left.\frac{dV_x(y)}{dy}\right|_{y=0}.$$

The stationarity condition $F_{\text{ac}} = F_{\text{fric}}$ allows one to relate $[dV_x(y)/dy]_{y=0}$ to the characteristic length L defined by Eq. (3.7):

$$\left.\frac{dV_x(y)}{dy}\right|_{y=0} = \frac{\nabla p}{\nu_0 L}.$$

In terms of the friction velocity U_τ, Eq. (1.7), and the friction Reynolds number Re, Eq. (1.8), this gives the famous constraint for wall-bounded flows

$$\left.\frac{dV_x(y)}{dy}\right|_{y=0} = Re\,\frac{U_\tau}{L}. \tag{3.8}$$

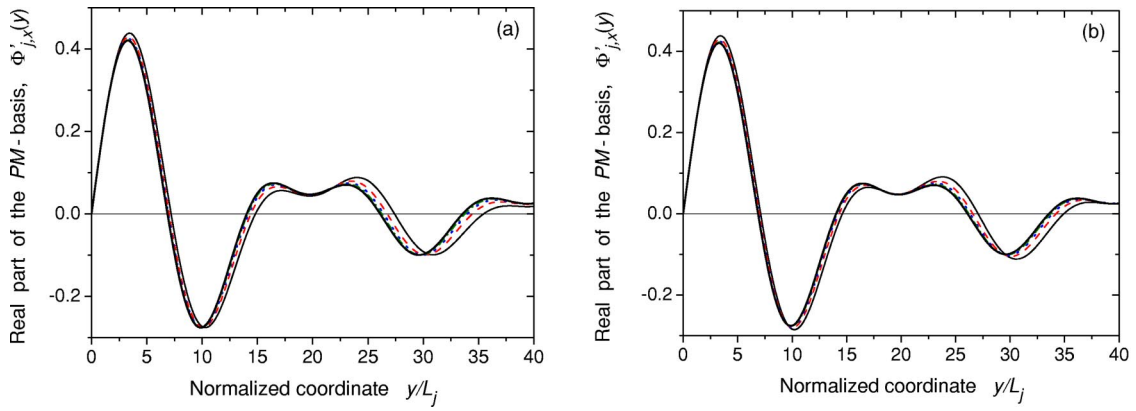

FIG. 4. Asymptotic universality of the *PM* basis functions. (a) Collapse of the rescaled real part of the basis functions $\Phi_j(2H\xi/\pi^2 2^j)$ for $n=5,\ldots,8$ with the universal asymptotic function $\Phi_{\text{un}}(\xi)$ for channel flow. The lines (from right to left) correspond to those in Fig. 3(c). The leftmost solid line denotes $\Phi_{\text{un}}(\xi)$. (b) The same for pipe flow, $H=R$.

TABLE I. Parameters of the *PM* basis for the planar and pipe geometries.

	Planar				Pipe			
j	s_j	$s_j 2^j$	R_j/H	ν_j/ν_0	s_j	$s_j 2^j$	R_j/R	ν_j/ν_0
1	0.811	1.62	0.50	6.48	0.692	1.38	0.51	2.77
2	0.122	0.49	0.77	1.96	0.185	0.74	1.03	1.48
3	0.038	0.30	0.90	1.22	0.068	0.54	1.00	1.09
4	0.015	0.25	0.95	0.99	0.029	0.47	1.00	0.94
5	0.007	0.22	0.98	0.89	0.014	0.44	1.00	0.87
6	0.003	0.21	0.99	0.85	0.007	0.42	1.00	0.84
7	0.002	0.21	0.99	0.83	0.003	0.41	1.00	0.82
8	0.001	0.21	1.00	0.82	0.002	0.41	1.00	0.82
∞		$2/\pi^2$	1	$8/\pi^2$		$4/\pi^2$	1	$8/\pi^2$

In all the mentioned global relationships the characteristic length L plays an important role.

Notice that for the channel of width $2H$ the length L is the distance from the centerline to a wall, $L=H$. For the pipe of radius R the length $L=R/2$, which is twice smaller than the distance from the center to the wall.

b. Zones in the channel and pipe. In Table I we present parameters s_j for the channel and pipe geometries, which are given by Eqs. (A4), (A13b), and (A14c).

Using s_j and L we introduce the *characteristic width of the j zone*:

$$L_j \equiv s_j L. \tag{3.9}$$

The idea behind this definition is that for the narrow near-wall zones L_j is exactly their geometrical width Δ_j, i.e., the distance between the j zone boundaries.

Assuming that Δ_j is much smaller than the local curvature of the boundary, we evaluate the area of a very narrow j zone as $S_j=\Delta_j P_\perp$. On the other hand, this area is $s_j S_\perp$. Therefore,

$$\Delta_j = s_j S_\perp / P_\perp = s_j L = L_j \quad \text{for } j \gg 1.$$

Obviously, for planar geometry, $\Delta_j = L_j$ for any j. To find the value of j at which the zones become flat, consider the pipe geometry with $\Delta_j = r_j - r_{j-1}$, where r_j is the radius of the circle occupied by the first j zones:

$$r_j = R\left[\sum_{i=1}^{j} s_i\right]^{1/2} \quad \text{(pipe)}. \tag{3.10}$$

Table II compares Δ_j/R given by this equation with $L_j/R = s_j/2$. Clearly, for $j>3$ these two parameters practically coincide.

TABLE II. Geometrical and characteristic widths Δ_j and L_j of j zone in pipe geometry.

j	1	2	3	4	5	6
Δ_j/R	0.83	0.105	0.0356	0.0148	0.0071	0.0035
L_j/R	0.35	0.093	0.0340	0.0145	0.0070	0.0035

4. Interpretation of the PM velocities

The *PM* expansions of the linear profiles [see Eq. (A9)], gives a simple interpretation of the velocities $V_j'(t)$ and $V_j''(t)$ as the $\hat{\mathbf{x}}$ and $\hat{\mathbf{e}}$ projections of $\mathbf{V}_{PM}(\boldsymbol{\rho},t)$ at some position within the j zone, ρ_j:

$$V_j'(t) \Leftrightarrow V_x(\rho_j,t), \quad V_x(\boldsymbol{\rho},t) \equiv \hat{\mathbf{x}}\cdot\mathbf{V}_{PM}(\boldsymbol{\rho},t), \tag{3.11a}$$

$$V_j''(t) \Leftrightarrow V_e(\rho_j,t), \quad V_e(\boldsymbol{\rho},t) \equiv \hat{\mathbf{e}}\cdot\mathbf{V}_{PM}(\boldsymbol{\rho},t), \tag{3.11b}$$

$$\hat{\mathbf{e}} \equiv \hat{\mathbf{x}} \times \boldsymbol{\rho}/\rho. \tag{3.11c}$$

This point will be illustrated below in Fig. 14 by direct comparison of V_j and $V(\boldsymbol{\rho})$ in appropriate coordinates.

C. Simple momentum equation for V_j

Consider the NSE for $\mathbf{V}_{PM}(\boldsymbol{\rho},t)$ in the form

$$\frac{\partial \mathbf{V}_{PM}(\boldsymbol{\rho},t)}{\partial t} = -\nu_0 \Delta \mathbf{V}_{PM} + \nabla p \hat{\mathbf{x}} - (\mathbf{V}_{PM}\cdot\boldsymbol{\nabla})\mathbf{V}_{PM} - \overline{(u\cdot\boldsymbol{\nabla})\mathbf{u}}. \tag{3.12}$$

Here ν_0 is the kinematic viscosity, and $\nabla p = -dp/dx > 0$ is the pressure gradient in the streamwise direction $\hat{\mathbf{x}}$. The nonlinear term $(\mathbf{V}_{PM}\cdot\boldsymbol{\nabla})\mathbf{V}_{PM}$ describes the self-nonlinearity in the *PM* subsystem and the last term $\overline{(\mathbf{u}\cdot\boldsymbol{\nabla})\mathbf{u}}$ is responsible for the effect of the Reynolds stress on the *PM* velocity. Here the overbar represents ensemble averaging in the sense of Eq. (2.9). The nonlinear cross term proportional to Vu (which has zero mean) is neglected.

The goal is to get the equation of motion for the complex *PM* velocities $V_j(t)$:

$$\frac{dV_j}{dt} = (\text{damping})_j + (\text{pressure})_j + (\text{self-interaction})_j + (\text{Reynolds stress})_j, \tag{3.13}$$

by projecting the NSE (3.12) on the *PM* basis, using Eqs. (A8) and (A12) in the form

$$V_j(t) = 2(\boldsymbol{\Phi}_j, \mathbf{V}_{PM})/(\boldsymbol{\Phi}_j, \boldsymbol{\Phi}_j). \tag{3.14}$$

Later in this section we derive the following equations for the terms in the RHS of Eq. (3.13):

$$(\text{damping})_j = -\Gamma_j V_j, \tag{3.15a}$$

$$(\text{pressure})_j = \nabla p, \tag{3.15b}$$

$$(\text{self-interaction})_j = 0, \tag{3.15c}$$

$$(\text{Reynolds stress})_j = W_j, \tag{3.15d}$$

$$W_j = d\kappa_j (u_{j-1}^2 - u_j^2).$$

Here Γ_j is given by Eq. (3.18) and the dimensionless parameter d characterize the strength of the interactions.

Collecting Eqs. (3.13), and (3.15), one finally gets the resulting momentum equation:

$$\frac{dV_j(t)}{dt} = -\nu_j \kappa_j^2 V_n + \nabla p + W_j, \tag{3.16}$$

where ν_j is the effective viscosity, given for the channel and pipe flows in Table I, and κ_j is given by Eq. (3.19). This equation together with Eq. (2.11) will be analytically and numerically analyzed in the following Secs. IV and V.

Readers not interested in the details of the derivation of Eqs. (3.15) can skip the rest of this section and proceed directly to Sec. IV.

1. The damping term

Projecting the NSE (3.12) on the real and imaginary parts of the *PM* basis Eq. (A2), and accounting only for the viscous term proportional to ν_0, one gets

$$\frac{dV_j'}{dt} = -\Gamma_j' V_j', \quad \frac{dV_j''}{dt} = -\Gamma_j'' V_j',$$

with, generally speaking, different Γ_j' and Γ_j'':

$$\Gamma_j' = -\nu_0 \frac{(\mathbf{\Phi}_j', \Delta \mathbf{\Phi}_j')}{(\mathbf{\Phi}_j', \mathbf{\Phi}_j')}, \quad \Gamma_j'' = -\nu_0 \frac{(\mathbf{\Phi}_j'', \Delta \mathbf{\Phi}_j'')}{(\mathbf{\Phi}_j'', \mathbf{\Phi}_j'')}. \tag{3.17}$$

However, in pipe flow they are equal, $\Gamma_j' = \Gamma_j''$, since the functions ϕ_m^+ and ϕ_m^- are the same; see Eq. (A14). In channel flow these functions, Eq. (A13), are different and hence $\Gamma_j' \neq \Gamma_j''$. Nevertheless, for large j, the basis functions $\Phi_j' \to \Phi_j''$ and $\Gamma_j' \to \Gamma_j''$. Therefore it would be a reasonable simplification to neglect the (possible) difference between Γ_j' and Γ_j'' and to write Eq. (3.15a) with the same damping term Γ_j, which is between Γ_j' and Γ_j''. For example, in channel flow, V_j' is responsible for the mean velocity profile $V_x(y)$ and thus "more important" than V_j''. In that case we will take $\Gamma_j = \Gamma_j'$. In planar Couette flow, the mean velocity profile is given by $V_z(y)$, which is connected to V_j'', and thus one had better take $\Gamma_j = \Gamma_j''$.

It is customary to represent the damping term via an effective viscosity ν_j and an effective wave vector κ_j, defined via the characteristic width of the j zone L_j:

$$\Gamma_j = \nu_j \kappa_j^2, \quad \nu_j \sim \nu_0, \tag{3.18}$$

$$\kappa_j \equiv \frac{1}{2L_j}, \quad L_j \equiv s_j L. \tag{3.19}$$

The parameters L and L_j were defined and discussed in Sec. III B 3 b. The values of s_j and ν_j for channel and pipe flows are presented in Table I.

Notice that the damping term in Eq. (3.15a) is diagonal in j. This is a consequence of our definition of the *PM* functions $\mathbf{\Phi}_j$, Eq. (A2): the functions with *different* j originate from different, and thus *orthogonal* eigenfunctions of the Laplace operator.

2. The pressure term

Equations (3.12) and (3.14) dictate

$$(\text{pressure})_j = 2\nabla p (\mathbf{\Phi}_j, \hat{\mathbf{x}})/(\mathbf{\Phi}_j, \mathbf{\Phi}_j).$$

Substituting $\hat{\mathbf{x}}$ from Eq. (A9a) into above expression, one gets Eq. (3.15b) for *any* flow geometry. This means that the pressure gradient uniform in $\boldsymbol{\rho}$ acts equally on all components $V_j'(t)$. This remarkable result could also be obtained from the interpretation of V_j, Sec. III B 4. Indeed, if we leave in the RHS of Eq. (3.12) only the pressure term, we get the ρ independent $V_x(\boldsymbol{\rho}, t) = \nabla p t$, i.e., a homogeneous velocity profile. This means that $V_j'(t)$ is independent of j.

3. The self-interaction term

In various simple flows the self-interaction term in Eq. (3.12) is identically equal to zero due to geometrical constraints. It is so for channel and planar Couette flows, where

$$(\mathbf{V} \cdot \boldsymbol{\nabla}) \mathbf{V} \Rightarrow \left(V_x \frac{\partial}{\partial x} + V_z \frac{\partial}{\partial z} \right) \mathbf{V}(y) \equiv \mathbf{0}.$$

Here we skipped for brevity the subscript *PM*. The same is true for pipe geometry, where

$$(\mathbf{V} \cdot \boldsymbol{\nabla}) \mathbf{V} \Rightarrow \left(V_x \frac{\partial}{\partial x} + \frac{V_\phi}{\rho} \frac{\partial}{\partial \phi} \right) \mathbf{V}(\rho) \equiv \mathbf{0}.$$

In the present paper we consider only flows with zero self-interaction, Eq. (3.15c).

4. Effect of the Reynolds stress

In the *PM* representation the Reynolds stress term in Eq. (3.13) should be a quadratic function of the turbulent velocities u_{nj} and should scale as $\kappa_j \equiv 1/(2L_j) \propto 2^j$. This term describes two physical processes, namely, (i) the exchange of linear and angular momenta between different zones and (ii), together with its counterpart w_j in the equation for u_{nj}, the energy exchange between V_j and u_{nj} subsystems.

In the spirit of the shell models of turbulence, we consider here the form of the Reynolds stress term that accounts for the momentum exchange only between nearest j zones (j and $j \pm 1$) and preserves the relevant integrals of motion, the energy, and the momenta. Notice that in turbulent channel and pipe flows with $\langle \mathcal{M} \rangle = 0$, the conservation of $\mathcal{P}$ is much more important that the conservation of $\mathcal{M}$. Therefore we can simplify the possible structure of the intersystem interaction terms W_j and w_j by using for $\mathcal{M}$ its simplified version, in which all R_j are assumed to be the same, $R_j \to R_\infty = \text{const}$, and thus can be omitted:

$$\tilde{\mathcal{M}} = \sum_j s_j V_j'' \Rightarrow (\text{quasiangular momentum}). \tag{3.20}$$

It is easily justified by noting that for $j>3$ the j zone contributions to $\mathcal{M}$ and $\tilde{\mathcal{M}}$ are almost the same (see Table I for R_j). In the following we will drop the tilde on $\tilde{\mathcal{M}}$, and write the quasiangular momentum simply as $\mathcal{M}$. Having in mind the conservation of the ''complex momentum''

$$\mathcal{L}\equiv\mathcal{P}+i\mathcal{M}=\sum_j s_j V_j,$$

we suggest the following form of the Reynolds stress term, W_j:

$$(\text{Reynolds stress})_j\equiv W_j=\frac{1}{s_j}(\mathfrak{p}_{j-1}-\mathfrak{p}_j), \qquad (3.21)$$

where $\mathfrak{p}_j$ is the momentum flux from the j to the $(j+1)$ zone. Indeed, this form provides the conservation of $\mathcal{L}$ in the inviscid, unforced limit:

$$\frac{d\mathcal{L}}{dt}=\sum_j s_j W_j=\sum_j (\mathfrak{p}_{j-1}-\mathfrak{p}_j)=0.$$

For the momentum flux $\mathfrak{p}_j$ we also select the simplest form, assuming that only the near-wall turbulent eddies of the same scale $u_{jj}\equiv u_j$ (i.e., u_{nj} with $n=j$) give a nonzero momentum transfer:

$$\mathfrak{p}_j=\frac{d}{2L}u_j^2. \qquad (3.22)$$

Equations (3.21) and (3.22) give us the simple Eq. (3.15d) for W_j.

The production term w_j, describing the energy pumping into the j zone of the turbulent subsystem Eq. (2.11), is then uniquely determined by the requirement of conservation of the total energy of the system:

$$w_j=\frac{d}{2\sigma_j L}(V_j-V_{j+1})u_j^*. \qquad (3.23)$$

IV. CONSERVATION LAWS AND SYMMETRIES IN THE MZS MODEL

A. Resulting dimensionless MZS equations

For the convenience of the reader we present here the full set of MZS equations which will be the subject of analytical and numerical studies. As the first step, we nondimensionalize the MZS equations, expressing time t and velocities V_j, u_{nj} in units of τ and U_τ:

$$\tilde{t}\equiv\frac{t}{\tau}, \qquad (4.1a)$$

$$\tilde{V}_j(\tilde{t})\equiv\frac{V_j(\tau\tilde{t})}{U_\tau}, \qquad (4.1b)$$

$$\tilde{u}_{nj}(\tilde{t})\equiv\frac{u_{nj}(\tau\tilde{t})}{U_\tau}, \qquad (4.1c)$$

$$\nabla\tilde{p}=1, \qquad (4.1d)$$

where the time τ and velocity U_τ are constructed from the ''outer'' characteristics of the flow, ∇p and L:

$$\tau\equiv\sqrt{L/\nabla p}, \quad U_\tau\equiv\sqrt{\nabla p L}. \qquad (4.2)$$

In the rest of the paper we omit the tildes on the dimensionless variables. The dimensionless MZS equations take on the form

$$\frac{dV_j}{dt}=-\Gamma_j V_j+\nabla p_j+W_j, \quad \nabla p_j=\nabla p=1, \qquad (4.3a)$$

$$\frac{du_{nj}}{dt}=-\gamma_n u_{nj}+\mathcal{N}_{nj}+\Delta_{nj}w_j, \qquad (4.3b)$$

$$j=1,2,\ldots,\infty, \quad n=j,j+1,\ldots,\infty.$$

Here the shell variables u_{nj} are the velocities of statistically identical (nj) eddies of characteristic scale s_n that belong to a j zone of width s_j. Clearly, in Eqs. (4.3b) $n\geqslant j$. The *PM* variables $V_j(t)$ describe the velocities of coherent near-wall structures in the j zone. In our notation the near-wall turbulent (nj) eddies have $n=j$. These eddies also occupy all j zones with $j\geqslant n$. Therefore, in our approach

$$u_{nj}=u_{nn}\equiv u_n \quad \text{for } j\geqslant n.$$

The terms on the RHS of the dimensionless MZS equations (4.3) are as follows:

$$\Gamma_j=\frac{G_j}{Re}\kappa_j^2, \quad \gamma_n=\frac{g_n}{Re}\kappa_n^2, \quad \kappa_j\equiv\frac{1}{2s_j}, \qquad (4.4a)$$

$$W_j=d\kappa_j(u_{j-1}^2-u_j^2), \qquad (4.4b)$$

$$w_j=\frac{d}{2\sigma_j}(V_j-V_{j+1})u_j^*, \quad \sigma_j\equiv\sum_{j'\geqslant j}s_{j'}, \qquad (4.4c)$$

$$\mathcal{N}_{nj}=N_{nj}+\Delta_{nj}\sum_{j'>j}\frac{s_{j'}}{\sigma_j}(N_{nj'}-N_{nj}), \qquad (4.4d)$$

$$N_{nj}=i(a\kappa_{n+1}u_{n+1,j}^*u_{n+2,j}+b\kappa_n u_{n-1,j}^*u_{n+1,j} -c\kappa_{n-1}u_{n-2,j}u_{n-1,j}). \qquad (4.4e)$$

Here

$$a+b+c=0, \quad \sum_{j\geqslant 1}s_j=1.$$

Equations (4.4) contain only one physical parameter, the friction Reynolds number

$$Re=LU_\tau/\nu_0, \qquad (4.5)$$

and a set of geometry dependent, dimensionless factors G_j, g_n, and s_j. For channel and pipe flows the factors $G_j = \nu_j/\nu_0$ and s_j are given in Table I. For simplicity in this paper we take $g_n = G_n$.

B. Conservation laws and fluxes

In the invisid ($\Gamma_j = \gamma_n = 0$), unforced ($\nabla p_j = 0$) limit Eq. (4.3) conserves energy $\mathcal{E}$, linear momentum $\mathcal{P}$, and (quasi) angular momentum $\mathcal{M}$:

$$\mathcal{E} = \frac{1}{2}\sum_{j=1}^{\infty} s_j \left(|V_j|^2 + \sum_{n=1}^{\infty} |u_{nj}|^2 \right), \tag{4.6a}$$

$$\mathcal{P} = \sum_{j=1}^{\infty} s_j V_j', \tag{4.6b}$$

$$\mathcal{M} = \sum_{j=1}^{\infty} s_j V_j''. \tag{4.6c}$$

In the general case, with nonzero Γ_j, γ_j, and ∇p_j the direct calculation of $d\mathcal{E}/dt$, $d\mathcal{P}/dt$, and $d\mathcal{M}/dt$ with the help of Eq. (4.3) gives

$$\frac{d\mathcal{E}}{dt} = \varepsilon^+ - \varepsilon^-, \tag{4.7a}$$

$$\frac{d\mathcal{P}}{dt} = \mathfrak{p}^+ - \mathfrak{p}^-, \tag{4.7b}$$

$$\frac{d\mathcal{M}}{dt} = \mathfrak{m}^+ - \mathfrak{m}^-. \tag{4.7c}$$

Here ε^+, $\mathfrak{p}^+$, and $\mathfrak{m}^+$, are *total* influxes of the respective integrals of motion, $\mathcal{E}$, $\mathcal{P}$, and $\mathcal{M}$, and ε^-, $\mathfrak{p}^-$, and $\mathfrak{m}^-$, are their *total* rates of dissipations. As for Eqs. (4.6) these objects can be represented as s_j-weighted sums $\Sigma_j s_j(\cdots)$ of the respective densities of *partial* influxes (ε_j^+, $\mathfrak{p}_j^+$, and $\mathfrak{m}_j^+$) and *partial* rates of dissipation in the j zone:

$$\varepsilon^+ = \sum_{j=1}^{\infty} s_j \varepsilon_j^+, \quad \varepsilon_j^+ = \nabla p_j V_j' = V_j', \tag{4.8a}$$

$$\mathfrak{p}^+ = \sum_{j=1}^{\infty} s_j \mathfrak{p}_j^+, \quad \mathfrak{p}_j^+ = \nabla p_j = 1, \tag{4.8b}$$

$$\mathfrak{m}^+ = \sum_{j=1}^{\infty} s_j m_j^+, \quad \mathfrak{m}_j^+ = 0, \tag{4.8c}$$

$$\varepsilon^- = \sum_{j=1}^{\infty} s_j \varepsilon_j^-, \quad \varepsilon_j^- = \Gamma_j |V_j|^2 + \sum_{n=1}^{\infty} \gamma_n |u_{nj}|^2, \tag{4.9a}$$

$$\mathfrak{p}^- = \sum_{j=1}^{\infty} s_j \mathfrak{p}_j^-, \quad \mathfrak{p}_j^- = \Gamma_j V_j', \tag{4.9b}$$

$$\mathfrak{m}^- = \sum_{j=1}^{\infty} s_j m_j^-, \quad m_j^- = \Gamma_j V_j''. \tag{4.9c}$$

The total influx of energy is exactly equal to the total linear momentum of the flow (due to our normalization $\nabla p = 1$) and the total influx of the linear momentum equals unity:

$$\varepsilon^+ = \nabla p \sum_{j=1}^{\infty} s_j V_j' = \nabla p \mathcal{P} = \mathcal{P}, \tag{4.10a}$$

$$\mathfrak{p}^+ = \nabla p \sum_{j=1}^{\infty} s_j = \nabla p = 1. \tag{4.10b}$$

For channel and pipe flows, the influx of angular momentum $\mathfrak{m}^+ = 0$. In planar Couette flow, $\mathfrak{p}^+ = 0$ and $\mathfrak{m}^+ \neq 0$.

Notice that the main part of the influx of momentum is always flowing into the first few zones, where s_j have considerable values. For example, in the channel, $\approx$81% of the total $\mathfrak{p}^+$ flows into the first zone (occupying $s_1 \approx 0.81$ part of the cross-sectional area; see Table I), 93% into the first two zones, and only about 1% to the fifth and all higher zones. As we show below, V_j' slightly decay with j; hence the influx of energy is even more confined to the first zones.

For very high Reynolds numbers the dissipation of the conserved quantities occurs at large j (or n), $\sim \log_2 Re$. Therefore for $\log_2 Re \gg 1$ there exists an inertial interval (generally speaking, different for the different quantities). Clearly, in the stationary case the influx of some conserved quantity has to be equal to its flux (in the shell space or via zones). For the energy, it is useful to analyze the flux in the shell space:

$$\varepsilon^+ = \varepsilon_n = \varepsilon^- = \mathcal{P}, \quad \varepsilon_n = \sum_{j=1}^{\infty} \varepsilon_{nj}, \tag{4.11}$$

where ε_{nj} is usual for shell model (in the j zone) expression of the flux of energy from the nth to the $(n+1)$th shell.

The flux of the linear momentum $\mathfrak{p}_j$ from the j to $(j+1)$ zone is given by Eq. (3.22), which in the dimensionless form reads $\mathfrak{p}_j = du_j^2/2$. Therefore, in the stationary case, for j in the inertial interval,

$$\mathfrak{p}_j = du_j^2/2 = \mathfrak{p}^+ = \mathfrak{p}^- = 1. \tag{4.12}$$

To get the expression for the value of $\mathfrak{p}_j$ valid for any j (not only in the inertial interval), we multiply Eq. (4.3a) by the j zone area s_j, and sum up from 1 to j. This gives the useful equation

$$\mathfrak{p}_j = du_j^2/2 = \sum_{i=1}^{j} s_i (1 - \Gamma_i V_i) \quad \text{for any } j, \tag{4.13}$$

which allows us to express the turbulent velocity $u_j = u_{jj}$, generating the turbulent energy cascade in the j zone, via *PM* velocities.

C. Galilean invariance of the model

The Galilean transformation to the reference system, moving with some velocity U_0 in the streamwise direction $\hat{\mathbf{x}}$, changes

$$\mathbf{V}(\rho,t)\underset{G}{\Rightarrow}\mathbf{V}(\rho,t)+\hat{\mathbf{x}}U_0.$$

According to Eqs. (A9a) and (3.14), it leads to the transformation:

$$V_j(t)\underset{G}{\Rightarrow}V_j(t)+U_0. \tag{4.14}$$

Clearly, the term w_j, Eq. (4.4c), describing the effect of the mean velocity on the turbulent subsystem, is Galilean invariant:

$$w_j=\frac{d}{2\sigma_j}(V_j-V_{j+1})u_j^*\underset{G}{\Rightarrow}w_j. \tag{4.15}$$

In other words, the uniform velocity profile $\mathbf{V}(\boldsymbol{\rho})=\hat{\mathbf{x}}\times\text{const}$ does not affect the statistics of turbulence. This important invariance of the MZS equations guarantees that for $\mathrm{Re}\to\infty$ the mean velocity profile in the core of the flow becomes uniform and the statistics of turbulence becomes space homogeneous, as expected.

D. Asymptotic scale invariance and equations for the turbulent boundary layer near a flat plane

Consider the MZS equation (4.3) at very large *Re* in the near-wall region, $n,j>j_*\gg1$, in which the dimensionless parameters in Eq. (4.4) can already be replaced by their asymptotic values:

$$G_j\Rightarrow G,\quad g_j\Rightarrow g,$$

$$s_j\Rightarrow 2^{-j}s,\quad \sigma_j=2s_j. \tag{4.16}$$

This is definitely so for channel and pipe flows, say, for $j_*=3$; see Table I. For large j the zone width is much smaller than the local curvature radius of the wall and the discussed situation corresponds to the case of a *turbulent boundary layer* (TBL) near a flat plane.

For $j\geqslant j_*$ the dimensionless flux of linear momentum from the j to $(j+1)$ zone, $\mathfrak{p}_j$, is very close to 1 and much larger than the direct influx into the j zone, $s_j\mathfrak{p}_j^+=s_j\ll1$ from the external pressure gradient. Therefore in this regime one can neglect in the RHS of Eq. (4.3a) $\nabla p=1$ with respect to W_j and simplify Eq. (4.3) to the scale invariant form

$$\frac{dV_j}{dt}=-\frac{G\kappa_j^2}{Re}V_j+d\kappa_j(u_{j-1}^2-u_j^2), \tag{4.17a}$$

$$\frac{du_{nj}}{dt}=-\frac{g\kappa_n^2}{Re}u_{nj}+N_{nj}+\frac{\Delta_{nj}}{2}\left[d\kappa_j(V_j-V_{j+1})u_j^*+\sum_{j'>j}2^{j-j'}(N_{nj'}-N_{nj})\right], \tag{4.17b}$$

$$\kappa_j=2^j\kappa,\quad \kappa=1/2s,\quad n\geqslant j\geqslant j_*, \tag{4.17c}$$

$$\mathfrak{p}^+=du_{j_*-2}^2/2=du_{j_*-1}^2/2=1, \tag{4.17d}$$

where N_{nj} already has the scale invariant form Eq. (4.4a). The "TBL boundary condition" at $j=j_*$, Eq. (4.17d), provides the influx of energy and mechanical momentum into the TBL, Eq. (4.17). In the initial Eq. (4.3) this role is played by the external pressure gradient $\nabla p=1$.

Equations (4.17) have additional [with respect to Eq. (4.3)] rescaling symmetry, namely, they remain unchanged under the transformation

$$V_j\to\tilde{V}_j=V_{j+j_0},$$

$$u_{nj}\to\tilde{u}_{nj}=u_{n+j_0,j+j_0},$$

$$t\to\tilde{t}=t/2^{j_0},$$

$$Re\to\widetilde{Re}=Re/2^{j_0}, \tag{4.18}$$

which corresponds (in the $\mathbf{r}$ space) to the simultaneous rescaling of the outer scale L and the pressure gradient ∇p in a way that leaves the value of the wall shear stress unchanged, $\nabla pL=\text{const}$. This symmetry of the equations means that the MZS model describes the asymptotic universality of the near-wall turbulence for $Re\to\infty$, and that the only relevant parameter in this regime is the total influx of the momentum $\mathfrak{p}^+$, which is fixed by the boundary conditions (4.17d).

In studies of the near-wall turbulence, it is customary to normalize the time and velocity units by the "inner" scales instead of the "outer" ones; namely, we should use the *viscous length scale* $\delta\equiv\nu_0/U_\tau=L/Re$ instead of the outer scale L, and the corresponding time scale $\tau_\delta\equiv\delta/U_\tau=\tau/Re$ instead of τ. As one can see, this rescaling corresponds to the choice $j_0=\log_2 Re$ in the transformation (4.18). In the new units, the MZS equations have the same form as Eq. (4.17) with $Re=1$:

$$\frac{dV_j}{dt}=-G\kappa_j^2V_j+d\kappa_j(u_{j-1}^2-u_j^2), \tag{4.19a}$$

$$\frac{du_{nj}}{dt}=-g\kappa_n^2u_{nj}+N_{nj}+\frac{\Delta_{nj}}{2}\left[d\kappa_j(V_j-V_{j+1})u_j^*+\sum_{j'>j}2^{j-j'}(N_{nj'}-N_{nj})\right], \tag{4.19b}$$

where we omit tildes on the new variables. Equations (4.19) represent the MZS model for a TBL near a flat plane.

Unlike Eqs. (4.17), in Eqs. (4.19) the zone and scale indices j and n can be both positive and negative: thus, V_0 corresponds to the velocity of the scale δ and V_{-1} to the structures of the scale 2δ, and so on.

We can use the general formulas (3.3) to reconstruct the mean velocity profiles $\mathbf{V}_{PM}(\boldsymbol{\rho})$. In this case the expression for $\mathbf{V}_{PM}(\boldsymbol{\rho})$ takes on an especially simple form, since all

functions $\mathbf{\Phi}_j(\boldsymbol{\rho})$ already have a scale invariant form. Taking into account our rescaling to the "inner" units, we can write

$$\mathbf{V}_{PM}(y)=Re\left[\sum_j V_j\Phi_{\rm un}(2^j\pi^2 y/2\delta)\right], \qquad (4.20)$$

where y is the distance to the wall, $\Phi_{\rm un}(\xi)$ is given by Eq. (3.6b), and $\mathbf{V}_{PM}(y)$ is measured in units of U_τ.

V. SOLUTION OF THE MZS EQUATIONS

A. Laminar velocity profile and its instability

1. Comparison of the full and PM laminar profiles

The simplest solution of the MZS equations (4.3), in which all $u_{nj}=0$, corresponds to laminar flow:

$$V_j=V_j^0\equiv\frac{1}{\Gamma_j}=\frac{\mathrm{Re}}{G_j\kappa_j^2}. \qquad (5.1)$$

Using Eq. (3.3), one reconstructs the laminar profile of the *PM* velocity:

$$\mathbf{V}_{PM}^0(\boldsymbol{\rho})=\sum_j V_j^0\mathbf{\Phi}_j'(\boldsymbol{\rho})=Re\sum_j\frac{\mathbf{\Phi}_j'(\boldsymbol{\rho})}{G_j\kappa_j^2}. \qquad (5.2)$$

The laminar profile of the full velocity $\mathbf{V}^0(\boldsymbol{\rho})$ satisfies the linear NSE, which in the dimensionless form (4.1) reads

$$\Delta\mathbf{V}^0(\boldsymbol{\rho})+\hat{\mathbf{x}}\,Re=\mathbf{0}. \qquad (5.3)$$

According to Eq. (A11) the *PM* velocity is understood as the *PM* projection of the full velocity: $\hat{\mathbf{P}}_{PM}\{\mathbf{V}(\boldsymbol{\rho})\}=\mathbf{V}_{PM}(\boldsymbol{\rho})$. Therefore, we expect that the laminar *PM* profile (5.2), satisfies the equation, similar to Eq. (5.3),

$$\hat{\mathbf{P}}_{PM}\{\Delta\mathbf{V}_{PM}^0(\boldsymbol{\rho})\}+\hat{\mathbf{x}}\,Re=\mathbf{0}. \qquad (5.4)$$

The proof of this equation is given in Appendix B.

In the case $\hat{\mathbf{P}}_{PM}\Delta=\Delta\hat{\mathbf{P}}_{PM}$ Eqs. (5.3) and (5.4) coincide, because $\hat{\mathbf{P}}_{PM}\mathbf{V}_{PM}=\mathbf{V}_{PM}$. If so, the functions $\mathbf{V}^0(\boldsymbol{\rho})$ and $\mathbf{V}_{PM}^0(\boldsymbol{\rho})$ have to coincide due to uniqueness of the solutions of Eq. (5.3) with zero boundary conditions. However, due to incompleteness of the *PM* basis, $\hat{\mathbf{P}}_{PM}\Delta\neq\Delta\hat{\mathbf{P}}_{PM}$, and hence the profiles $\mathbf{V}^0(\boldsymbol{\rho})$ and $\mathbf{V}_{PM}^0(\boldsymbol{\rho})$ are expected to differ. In other words, Eq. (5.2) cannot reconstruct *exactly* the laminar profile $\mathbf{V}^0(\boldsymbol{\rho})$. This is the price to pay for the incompleteness of the *PM* basis. Nevertheless the *PM* basis is "full enough" to allow the reconstruction of any "physically possible" mean velocity profile with good accuracy. As a first demonstration of this fact we compare in Fig. 5 the exact and the *PM laminar* profiles for channel flow, which differ only by a few percent. This small loss of accuracy is insignificant with respect to a dramatic simplification of the calculation scheme for $\mathbf{V}(\boldsymbol{\rho},t)$: for large *Re* the mean velocity field in *PM* representation has $N\approx\ln Re$ significant coefficients V_j, while in the corresponding complete cell basis one has to account for $\sim Re\gg N$ functions.

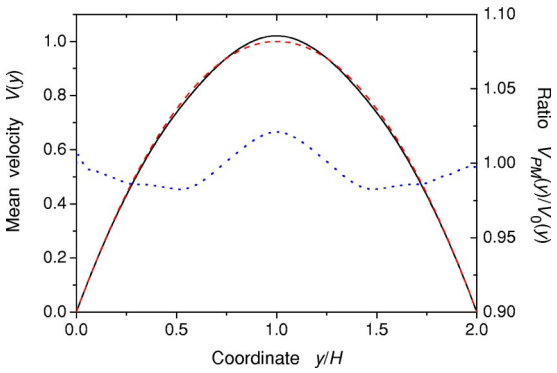

FIG. 5. Comparison of the exact (solid line) and *PM* (dashed line) laminar profiles for channel flow. The ratio of the two profiles is shown by the dotted line. Its values are marked on the right axis.

2. Instability of the laminar flow at $Re=Re_{cr}$

The laminar solution (5.1) exists for all *Re*. For large *Re*, however, it becomes unstable with respect to excitation of turbulent near-wall eddies u_j. A simple analysis of the linearized Eq. (4.3b) (i.e., $\mathcal{N}_{nj}\Rightarrow 0$) shows that the instability condition of the j eddy reads

$$\gamma_j<d(V_j-V_{j+1})/2\sigma_j. \qquad (5.5)$$

Substituting here V_j from Eq. (5.1) one gets

$$\frac{g_j\kappa_j^2}{Re}<\frac{d}{2\sigma_j}\left(\frac{1}{G_j\kappa_j^2}-\frac{1}{G_{j+1}\kappa_{j+1}^2}\right)Re,$$

which can be rewritten as the condition for *Re*:

$$Re>Re_j\equiv\kappa_j^{3/2}\sqrt{\frac{\sigma_j}{s_j}\frac{g_jG_jG_{j+1}}{d(G_{j+1}-G_j\kappa_j^2/\kappa_{j+1}^2)}}. \qquad (5.6)$$

It is clear that $Re_j\propto\kappa_j^{3/2}$; therefore, usually the first unstable zone is the first one, $j=1$.

We want to stress that Eq. (5.6) gives a correct instability threshold only for the *first* unstable zone:

$$Re_{\rm cr}=Re_1=\kappa_1^{3/2}\sqrt{\frac{\sigma_1g_1G_1G_2}{s_1d(G_2-G_1\kappa_1^2/\kappa_2^2)}}. \qquad (5.7)$$

The excitation of turbulence in, say, the first zone will lead to a significant momentum flux from the first to the second zone. As a result, the mean velocity V_2 will increase, the second zone velocity gradient V_2-V_3 will increase too, and the instability condition for u_2 will be therefore satisfied for smaller Reynolds numbers than predicted by Eq. (5.6). We will show later that the real instability threshold for the jth zone is proportional to $Re_j\propto\kappa_j$, i.e., is much smaller than the "laminar" result (5.6).

B. Wall-bounded flows in the approximation of near-wall eddies ($a=b=c=0$)

In Sec. IV A we found the laminar solution of the MZS equations (4.3) with $u_{nj}=0$ and showed that this solution becomes unstable at $Re=Re_{\rm cr}$ with respect to excitation of

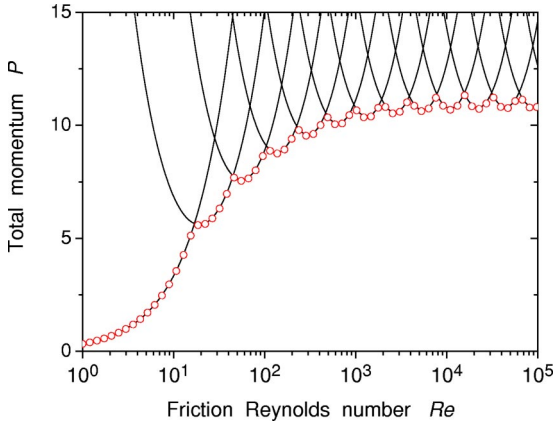

FIG. 6. Total momentum of the flow vs. the Reynolds number *Re*. Circles denote numerical data for the channel flow, $d=0.046$; solid lines the analytical prediction [Eq. (C5)] for different number of unstable zones m, $m=1,2,...$ (from left to right).

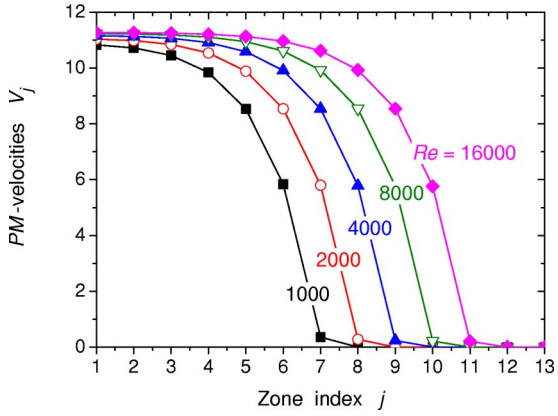

FIG. 7. Mean zone velocities V_j vs the zone index j for different Reynolds numbers *Re*.

the near-wall velocity $u_1 \equiv u_{11}$. As the next step in this section we analyze a much more general solution of Eqs. (4.3), that allows nonzero values of all near-wall velocities, $u_{jj} \equiv u_j$. The jj eddies can be excited by a direct interaction with the *PM* velocities V_j. To prohibit turbulent cascades leading to excitation of other nj eddies (with $n>j$), one can neglect in Eq. (4.3b) the interaction term $\mathcal{N}_{nj}$ (i.e., put $a=b=c=0$). In this case the MZS equations (4.3) take on a simple form:

$$\frac{dV_j}{dt} = -\Gamma_j V_j + 1 + d\kappa_j (u_{j-1}^2 - u_j^2), \tag{5.8a}$$

$$\frac{du_j}{dt} = -\gamma_j u_j + \frac{d}{2\sigma_j}(V_j - V_{j+1}) u_j^* . \tag{5.8b}$$

The solution of these equations in the stationary regime ($d/dt=0$) is presented in Appendix C. Note that this rather complicated case can be solved *analytically* in the MZS approach. The main results of the analysis are as follows.

(1) The jth turbulent velocity becomes unstable at Reynolds number $Re_j \propto \kappa_j$, which is much smaller than the critical Reynolds number (5.6) estimated on the analysis of the linear stability problem. For large enough *Re* the number of nonzero, unstable turbulent velocities is $m(Re) \sim \log_2 Re$.

(2) The total momentum $\mathcal{P}$ of the flow (i.e., total flux of the fluid) *does not grow infinitely as* $Re \to \infty$, but goes to some finite value. In other words, neglecting the dissipation of energy in turbulent cascades, one concludes that with the given cross-sectional area of the flow and pressure gradient, the total flux of the fluid reaches some limit in spite of the infinite decrease of the kinematic viscosity. The numerical and analytical calculations for the channel geometry, shown in Fig. 6, support this unexpected conclusion. In Fig. 6 one sees small oscillations of $\mathcal{P}$ with period $\Delta(\log_2 Re)=1$; this effect is an artifact of model discretization with spacing parameter $\lambda=2$ and has no physical meaning.

The reason for such strange behavior of $\mathcal{P}(Re)$ is that the stationary zone velocity differences ΔV_j in the unstable region $j<m$ are determined solely by the dissipation of turbulent eddies γ_j [see Eq. (C2)] that go to zero as $Re \to \infty$ (for finite j). Thus, in the limit $Re \to \infty$, $\Delta V_j \to 0$ and $V_j \to$ const. This conclusion is illustrated in Fig. 7. Clearly, for large *Re* the first few velocities remain unchanged, and the only effect of increasing *Re* is the shift of the "dissipative cutoff" towards the smaller scales. However, the total momentum is determined mainly by the first few zones and thus remains the same.

This analysis shows importance of the turbulent cascade for the experimentally observed characteristics of real flows, i.e., infinite increase of the total flux, logarithmic profiles, etc. The stationary condition $\Delta V_j = \Delta V_j^{\rm cr}$ will hold even if one accounts for a turbulent cascade, which adds some *turbulent damping* γ_j^T for turbulent near-wall eddies instead of the usual one γ_j. The turbulent damping *does not vanish in the limit* $Re \to \infty$. Thus, one obtains $\Delta V_j = \Delta V_j^{\rm cr} \neq 0$, and the total momentum will infinitely increase, as it is shown in Sec. IV C.

C. Wall-bounded flows in the turbulent viscosity approximation

In this section we show that even a rough account of the turbulent cascade in the MZS model already gives qualitatively correct analytical results.

1. MZS equations in the turbulent viscosity approximation

In the fully developed turbulent regime, the action of the interaction term $\mathcal{N}_{nj}$ on the eddy u_{nj} can be approximately accounted for in the "turbulent viscosity" approximation in which the energy flux from the energy containing jj eddies toward small scales in the j zone is replaced by a nonlinear damping term, ensuring the same loss of their energy. Formally, this can be done by replacing the nonlinear term $\mathcal{N}_{jj}$ in the full MZS equations (4.19) by some effective turbulent damping term γ_j^T:

$$\mathcal{N}_{jj} \Rightarrow -\gamma_j^T u_j, \quad \gamma_j^T = \alpha \kappa_j |u_j|, \tag{5.9a}$$

$$\alpha \approx (a-c). \tag{5.9b}$$

Here γ_j^T is chosen as the turnover frequency of *jj* eddies, $\kappa_j|u_j|$ with some dimensionless prefactor α. This prefactor is evaluated in Eq. (5.9b) by equating the total rate of energy dissipation in the model system with the effective turbulent damping (5.9a) and the energy flux toward small scales in the full shell model (see, e.g., Ref. [3]).

In the suggested *effective turbulent damping* approximation, the MZS equations (4.19) take the form

$$\frac{dV_j}{dt} = -\Gamma_j V_j 1 + d\kappa_j(u_{j-1}^2 - u_j^2), \tag{5.10a}$$

$$\frac{du_j}{dt} = -(\gamma_j + \alpha\kappa_j|u_j|)u_j + \frac{d}{2\sigma_j}(V_j - V_{j+1})u_j^* . \tag{5.10b}$$

These equations are different from the MZS equations in the near-wall eddy approximation, Eq. (5.8), by only the term proportional to α.

For large *Re* in the near-wall region Eq. (5.10) has a simpler, scale invariant form, in which all geometry dependent factors are taken in their small scale limit (4.16):

$$\frac{dV_j}{dt} = -\frac{G\kappa_j^2}{Re}V_j + 1 + d\kappa_j(u_{j-1}^2 - u_j^2), \tag{5.11a}$$

$$\frac{du_j}{dt} = -\left(\frac{g\kappa_j}{Re} + \alpha|u_j|\right)\kappa_j u_j + \frac{d\kappa_j}{2}(V_j - V_{j+1})u_j^* , \tag{5.11b}$$

where $\kappa_j = 2^j/2s$.

2. Inertial interval solution

In this section we consider the stable stationary solution of Eq. (5.10),

$$V_j = \frac{2\sqrt{2}\alpha}{d^{3/2}}[q(Re) - j] + \frac{\sqrt{d}}{\sqrt{2}\alpha}\frac{g}{G}, \quad j > 3, \tag{5.12}$$

obtained in Appendix D.

Notice that the only *Re* dependent factor in Eq. (5.12) is the position of the viscous cutoff $q(Re)$, given by the Eq. (D6b). Counting j from $q(Re)$, one has Re independent *PM* velocities. In the physical space this corresponds to the universality of the TBL profile measured in the "wall units" $y^+ = y\,Re$.

One can easily see that the set of zone velocities (5.12) linear in j in the inertial interval corresponds to the logarithmic profile of the mean velocity in the physical space: $V(y) \sim \ln(y\,Re/L)$. Actually, by a direct calculation one shows that the logarithmic profile

$$V^{\log}(y) = \frac{1}{\kappa_K}\ln\left(\frac{y\,Re}{L}\right) + B, \tag{5.13}$$

corresponds to the zone velocities

$$V_j^{\log} = \frac{\ln 2}{\kappa_K}(\log_2 Re - j) + \left(B - \frac{1 + \gamma_E - \ln(4/\pi)}{\kappa_K}\right) \simeq \frac{0.69}{\kappa_K}(\log_2 Re - j) + B - \frac{1.34}{\kappa_K}, \tag{5.14}$$

where $\gamma_E \simeq 0.58$ is the Euler gamma constant.

Thus, the MZS model describes the transition to the universal logarithmic profile with the von Kármán constant

$$\kappa_K = \frac{\ln 2}{2\sqrt{2}}\frac{d^{3/2}}{\alpha} \simeq 0.25\frac{d^{3/2}}{\alpha}. \tag{5.15}$$

D. Numerical analysis of the turbulent channel flow in the MSZ model

This section is devoted to the numerical analysis of the MZS model of channel flow in the effective turbulent damping approximation, Eq. (5.10). For simplicity we adopt $g_j = G_j$. The *PM* damping factor G_j was found according to Eq. (3.17) as the matrix elements of the viscous operator on the real part of the *PM* basis $\Phi_j'(y)$. This gives

$$G_j = 2^{j+2}s_j .$$

The parameters $d = 4.6\times10^{-2}$ and $\alpha = 5.9\times10^{-3}$ were chosen to reproduce the experimental values of the universal constants $\kappa_K \approx 0.4$ and $B \approx 5.2$.

In numerical analysis, 30 zones were sufficient to describe the flows with Reynolds number up to 10^9. In order to find the stationary solution of the full MSZ equations (5.10) we develop extremely stable and efficient iteration procedure, based on the essential physics of the problem; see Appendix E. In spite of the huge Reynolds numbers, the accuracy better than 10^{-6} was reached with about 100–200 iterations. Actually, using our approach the (MZS model and the iteration procedure) one can simulate turbulent wall-bounded flows for *arbitrarily large Re* with a very modest PC, even with a XT486PC at 40 MHz, 8 Mbytes of RAM.

1. Behavior of the zone velocities V_j and u_j

In Fig. 8, left panel, we plot *PM* velocities V_j for different *Re* from 500 to 5×10^8. One clearly sees the inertial interval, where V_j decrease linearly with j in agreement with Eq. (D2). As we mentioned above there is a "soft" viscous cutoff, that involves last two zones. In order to demonstrate the phenomenon of universality, in the right panel of Fig. 8 we replot the same velocities V_j as functions of the "near-wall" zone index $j - \log_2 Re$ as suggested by Eq. (5.12). There is a perfect collapse of all lines. Importantly, they collapse not only in the inertial interval, but also in the dissipative cutoff range. There is a non-negligible difference for the first two to three zones, $j = 1,2$ (see the inset in the right panel) that is caused by the non-negligible momentum influx in these zones. This deviation is described by Eq. (D2).

Figure 9 shows the magnitudes of the near-wall turbulent eddies $|u_j|$ for the same set of *Re*'s. Again, the numerical results are in full agreement with our theoretical understand-

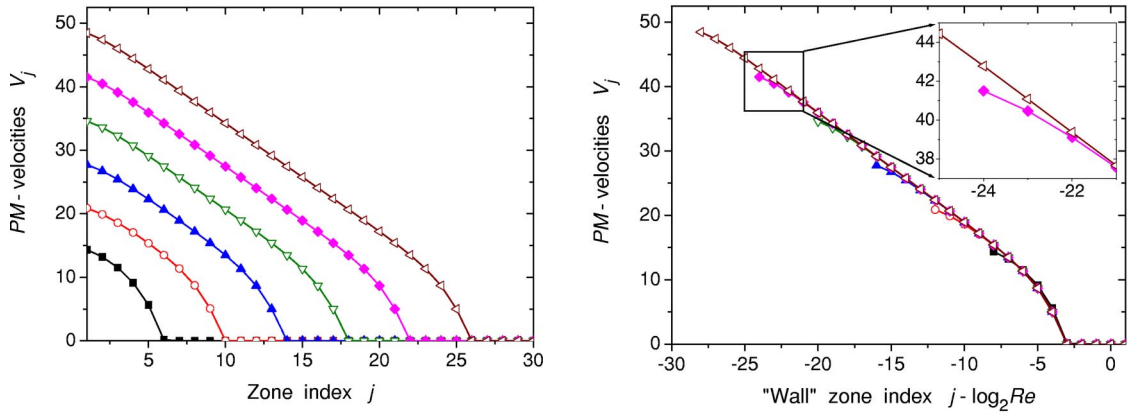

FIG. 8. *PM* velocities V_j for different Reynolds numbers *Re* as a function of the zone index j (left panel) and of the "near-wall" zone index ($j-\log_2 Re$) (right panel). The lines from lower to upper correspond to $\log_2 Re=9$, 13, 17, 21, 25, and 29, respectively.

ing: the magnitudes of the near-wall eddies in the inertial interval are constant, as it required by Eq. (D5) from the condition of the constancy of momentum flux. At the dissipative cutoff we observe a decrease of u_j involving 3–4 zones. A small decrease of u_j at the first few shells is caused by the nonzero momentum flux into these zones; in this region u_j with good accuracy can be found from

$$\mathfrak{p}_j = d u_j^2/2 = 1-\sigma_{j+1}. \tag{5.16}$$

To check how the approximation of turbulent viscosity, Eq. (5.9), affects the resulting mean velocity profile we compare in Fig. 10 the solutions of the full MZS equations (4.19) (black squares) and MZS equations (5.10) in the approximation of turbulent viscosity, Eq. (5.9) (empty circles). These solutions practically coincide except for three zones ($j=12,13,14$) near the viscous cutoff. In these zones just a few shells are excited in the full model (4.19) and the observed difference is an artifact of discreteness of the scale space in the shell models [recall that in the shell model (4.19) the spacing parameter $\lambda=2$]. In the case when the details of turbulent cascades near the wall are physically important (e.g., in turbulent flows with polymeric additives) one has to use more detailed shell representation of turbulent velocity field, say with $\lambda=\sqrt{2}$ or even $\lambda=2^{1/4}$, preserving the interaction range in the scale space unchanged. This modification of our model is under construction and will be published elsewhere.

We expect that more detailed models with $\lambda<2$ will give the mean profile closer to that given by the reduced model with turbulent damping (5.10), in which the energy dissipation is affected by the scale spacing. In this paper we are not interested in details of turbulent cascades and will use further only Eqs. (5.10).

2. Reconstruction of the mean velocity profile

Equation (3.3) reconstructs *PM* velocity profile $V_{PM}(y)$ from the set of V_j. For the case of the channel flow one has

$$V_{PM}(y)=\sum_{j=1}^{\infty} V_j \Phi_j'(y),$$

$$\Phi_j'(y)=\sum_{m=2^{j-1}}^{2^{j-1}} p_m \phi_{2m-1}(y), \tag{5.17}$$

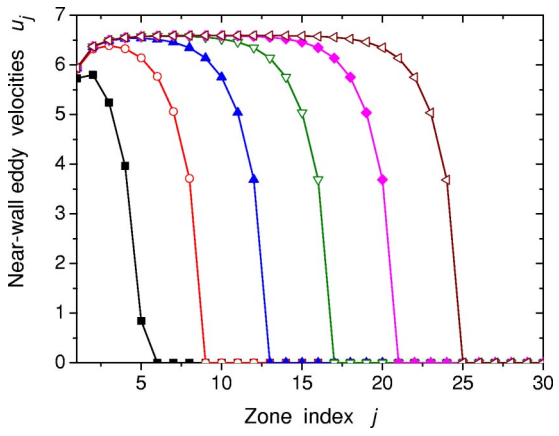

FIG. 9. Magnitude of the near-wall turbulent eddies $|u_j|$ as a function of the zone index j for different *Re*. The lines are marked as in Fig. 8.

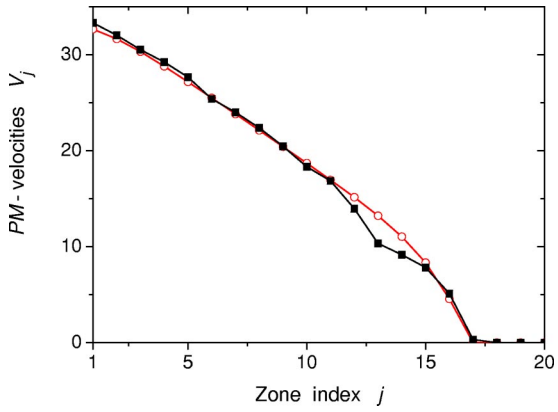

FIG. 10. Comparison of numerical solutions of the full MZS equations (4.19) (black squares) and the MZS equations (5.10) in the approximation of turbulent viscosity (5.9) (empty circles). $Re=10^6$.

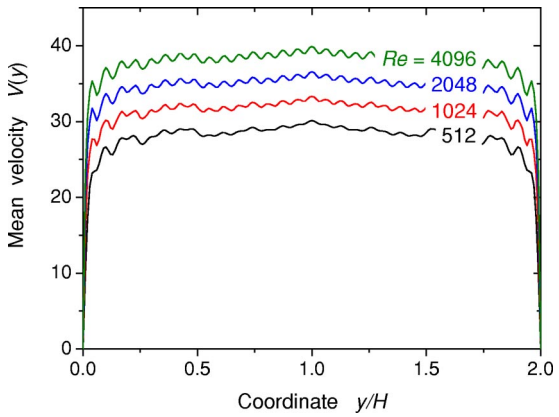

FIG. 11. Reconstructed *PM* velocity profiles $V_{PM}(y)$ for different Reynolds numbers.

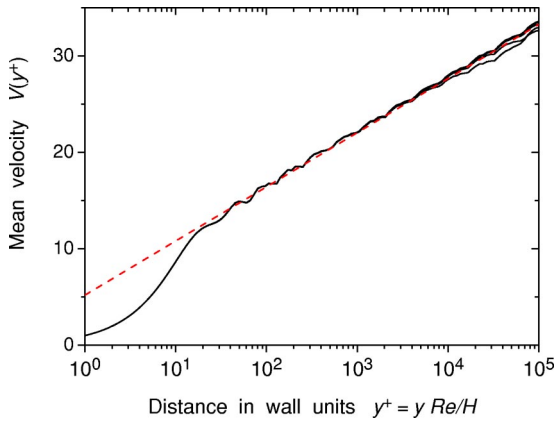

FIG. 12. Collapse of the mean velocity profiles in the near-wall units. Different lines (from below to above) correspond to $Re=2^{17}\sim 1.3\times 10^5$, 2^{21}, 2^{25}, and $2^{29}\sim 5\times 10^8$.

where p_m and $\phi_m(y)$ for channel geometry are given by Eq. (A13). The results of such reconstruction for a set of *Re*'s are shown in Fig. 11. We see that reconstructed *PM*-profiles show all qualitative features of the ''real'' mean velocity profiles in the well-developed turbulent regime; namely, the mean *PM* velocity is almost constant in the main part of the flow [with centerline velocity increasing with *Re* as ln(Re)]. As expected, all fall of $V(y)$ occurs in a small region near the walls. It is also clear that the width of this near-wall region decreases as *Re* increases, in the same way as in real flows.

Figure 11 shows that the *PM* profiles have some nonphysical ''wiggles.'' They originate from the incompleteness of the *PM* basis. Indeed, the *PM* basis is constructed by Eq. (A2) from the complete ϕ basis with some prescribed m dependence for each j function. As a result, the *PM* expansion (5.17) can be understood as the Fourier expansion in $\phi_m(y)\propto\sin(k_{2m-1}-y)$ with discontinuities of the Fourier amplitudes at the ''zone boundaries'' $m=2^j$, which produces the wiggles in the y representation. This artifact of the model can be removed in different ways. The simplest one is to add some function $\tilde{V}(y)$, orthogonal to all *PM* basis functions (and thus having zero momentum), the amplitude and the shape of which are determined from the problem of minimization of discontinuities in the spectrum. It can be shown that the result of such a ''smoothing'' is fully acceptable for most purposes.

Figure 12 displays the *PM* velocities in the near-wall region $y\ll H$ in log-linear scale for different *Re*'s from $\sim 1.3\times 10^5$ to $\sim 5\times 10^8$. The distance from the wall is measured in near-wall viscous lengths, $y^+=y/\delta=y\,Re/H$. The collapse of profiles for different Reynolds numbers is evident. One can see the viscous sublayer (for $y^+\leqslant 10$) and universal logarithmic profile (for $y^+\geqslant 50$).

3. Comparison of the MZS universal mean velocity profile with experiment and DNS results

In Fig. 13 we compared the reconstructed MZS universal mean velocity with the DNS results in a channel, Ref. [19] and with the laboratory measurements at *Re* up to 3.5×10^7, presented in Ref. [20]. The DNS data are available for $y^+<100$, while the experimental data are obtained for $y^+>10$. As expected, in the overlap region, $10<y^+<100$, both results collapse. As we explained, our MZS model reproduces the asymptotical logarithmic profile (5.13), and the parameters of the model, α and d were chosen to give known values of κ_K and B, that parametrize Eq. (5.13). Therefore, as expected, the MZS profile, displayed in Fig. 13 as a solid line, coincides with the experimental date in the region of large enough y^+. The point is that the MZS dependence $V_{PM}(y^+)$ practically coincides with the DNS and experimental data in all regions of y^+. It means that the MZS model correctly describes the basic physics that affects the mean velocity profile in the universal near-wall region of turbulent boundary layer near the flat plane. The MZS description of the viscous and the buffer layers *does not require adjustable parameters*.

4. Reconstruction of the profile of the energy dissipation

The total dissipation rate ε_j^- in j-zone, Eq. (4.9a), can be split into the dissipation rate in the *PM* velocity subsystem $\tilde{\varepsilon}_j^-$ and the dissipation rate in the turbulent subsystem $\hat{\varepsilon}_j^-$:

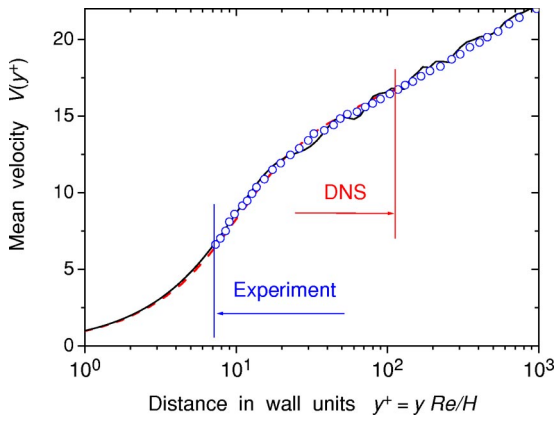

FIG. 13. Comparison of the reconstructed MZS universal mean velocity profile $V(y^+)/U_\tau$, (solid line in the region $1\leqslant y^+\leqslant 10^3$) with the DNS results in a channel, available in Ref. [19] for $y^+<10^2$ (dashed line), and with the measurements in a pipe, taken from Ref. [20] for $y^+>10$ (empty circles).

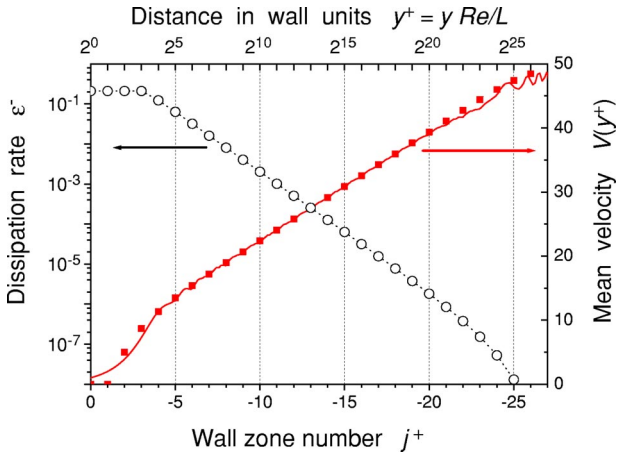

FIG. 14. Mean velocities V_{j^+} (black squares) and turbulent dissipation rates $\varepsilon^+_{j^+}$ (empty circles) in the wall-zone representation j^+, introduced by Eq. (5.20). Solid line, reconstruction of the *PM* velocity profile (in wall units) $V_{PM}(y^+)$ vs distance y^+ in wall units, shown above. $Re=5\times10^8$.

$$\varepsilon_j^- = \tilde{\varepsilon}_j^- + \hat{\varepsilon}_j^-,$$

$$\tilde{\varepsilon}_j^- = \Gamma_j |V_j|^2, \quad \hat{\varepsilon}_j^- = \sum_{i\leqslant j} \gamma_{\mathrm{ef},i} |u_i|^2. \tag{5.18}$$

In the turbulent viscosity approximation the effective damping is given by

$$\gamma_{\mathrm{ef},j} = \gamma_j + \alpha\kappa_j |u_j|. \tag{5.19}$$

Figure 14 displays as empty circles the dissipation density in turbulent subsystem, normalized by the near-wall length scale, i.e., $\hat{\varepsilon}_j^-/Re$ as a function of the "wall zone number" defined here as

$$j^+ \equiv j - \log_2 Re + 2. \tag{5.20}$$

The black squares in this figure show the *PM* velocities in the "wall-zone" representation, i.e., values of V_{j^+} for the same $Re=5\times10^8$. The solid line is the logarithmic plot of the reconstructed (from this set of V_j) *PM* velocity in the physical space, i.e., $V_{PM}(y^+)$ vs $\log_2 y^+$, shown from above. As one sees, the solid line goes very close to the black squares, as it should according to the interpretation of the *PM* velocities V_{j^+} as a "physical" velocity at some point within j^+ zone, as explained in Sec. III B 4. As is clear from Fig. 14, the wall zone numbers (5.20) are chosen to give a very simple "correspondence rule":

$$\text{wall zone index } j^+ \Leftrightarrow \text{wall distance } y^+ = 2^{-j^+}. \tag{5.21}$$

This approach can be used to restore the spatial distribution of various turbulent characteristics. In particular, we can understand $\varepsilon^-_{j^+}$, presented in Fig. 14, as $\varepsilon^-(y^+)$ with $y^+ = (2^{-j^+})$. As expected, the dissipation rate (normalized, as in Fig. 14, by *Re*) is *Re* independent as $Re\to\infty$. In this sense, the results in Fig. 14 can be considered as universal. As

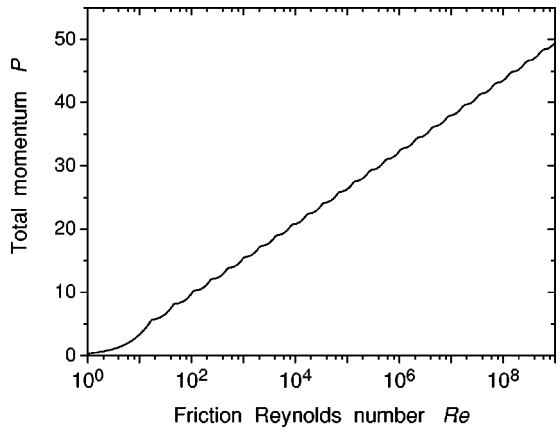

FIG. 15. Dependence of the total momentum of the flow $\mathcal{P}$ on the Reynolds number *Re* in channel flow.

expected, at large *Re* the main energy dissipation occurs in a narrow near-wall region, $y^+<40$. The dissipation rate at the wall in our model is equal to

$$\varepsilon|_{\mathrm{wall}} = \lim_{j\to\infty} \hat{\varepsilon}_j^-/Re \approx 0.21, \quad Re>10^4, \tag{5.22}$$

which is reasonably close to the result for smaller *Re*, available in the DNS of Ref. [21]:

$$\varepsilon|_{\mathrm{wall}} = 0.166, \quad Re\sim 200. \tag{5.23}$$

Notice the difference in *Re*'s and that our result (5.22) is obtained in the simple model with just two adjustable parameters, chosen to adjust very different characteristics of the flow, the mean velocity profile. This allows one to consider the reasonable correspondence of Eqs. (5.22) and (5.23) as an argument in favor of our simple MZS model.

5. Re dependence of the global flow characteristics

Clearly, our approach allows one to evaluate various global characteristics of the turbulent wall bounded flows.

The first example is the *Re* dependence of the total momentum (i.e., total flux) of the flow, shown in Fig. 15. There is a laminar regime for $Re<17$, and a developed turbulent regime for, say, $Re>100$. The "period-2" oscillations are an artifact of the model, caused by the discretization with the spacing parameter $\lambda=2$. These oscillations, however, are small and should be ignored. In principle, they can be removed in more "advanced" versions of the MZS model with few variables in each j zone, $V_{j,\sigma}, u_{j,\sigma}$, responsible for σ subzones of the j zone.

The second example is the *Re* dependence of the total energy of the system, as well as parts of the energy, containing in the mean and turbulent subsystems, shown in Fig. 16.

The last, but not least, example is the *Re* dependence of the total energy dissipation and that for the *V* and *u* subsystems, shown in Fig. 17. Total energy dissipation is equal to the total energy influx, i.e., to the total momentum of the flow. However, the distribution of energy dissipation between two subsystems is very interesting.

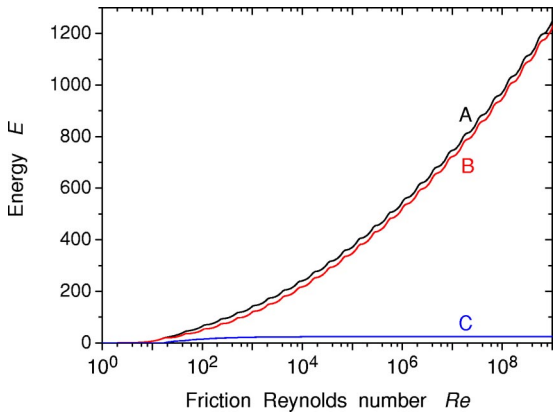

FIG. 16. Dependence of the total energy (A), the energy of the mean V-subsystem (B), and the energy of the turbulent u subsystem (C) on the Reynolds number Re.

One clearly sees that some flow characteristics, like the energy of the turbulent subsystem and the energy dissipation in the mean flow subsystem remain finite for vanishing fluid viscosity ν_0. At the same time, other characteristics, such as the total linear momentum, the energy of the mean flow subsystem, and the rate of energy dissipation increase infinitely [like $\ln(1/\nu_0)$], i.e., demonstrate a phenomenon of *viscous anomaly*. The MZS model clearly demonstrate that the physical reason for that anomaly is the separation in the physical space of the external forcing and the friction: the external pressure gradient, that accelerates the flow, acts on the whole cross-sectional area of the flow, while the friction force, that prevents the mean velocity from infinite growth, acts only on the walls. To be able to maintain the constant flux of the linear mechanical momentum toward the wall, the amplitudes of the near-wall eddies of all scales, u_j, must be j independent. This immediately leads to a linear increase of V_j with j, decreasing from the viscous cutoff value j_0 toward the beginning of the cascade $j=1$. Thus the value of V_1 is proportional to the total number of cascade steps, j_0-1. Decrease of ν_0 to one-half of its value adds one more step in the inertial interval of the momentum cascade. This leads to an increase of V_1 by $\sim \ln 2$. In dimensional units this corresponds to the increase of V_1 by $\sim V_\tau \ln 2 \sim \ln 2 \sqrt{L \nabla p}$.

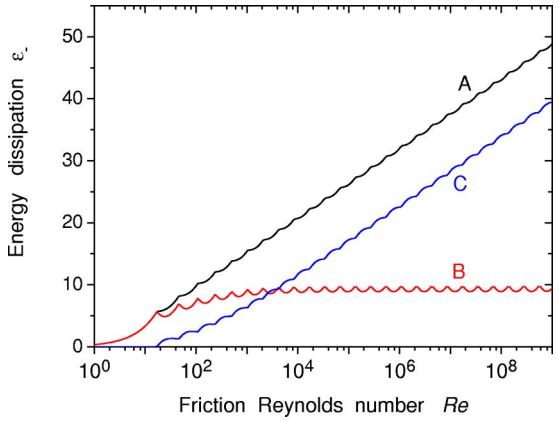

FIG. 17. Dependence of the total energy dissipation (A), energy dissipation in the mean V subsystem (B), and energy dissipation in the turbulent u subsystem (C) on the Reynolds number Re.

VI. SUMMARY

We developed a multizone shell model for wall-bounded turbulent flows in a piecewise approximation, dividing the cross-sectional area into a set of $N \sim \log_2 Re\, j$ zones. In each zone the turbulence is assumed to be homogeneous and is described in the framework of a shell model equation for the "turbulent" shell velocities $u_{nj}(t)$. The mean velocity is described by an additional set of N zone variables $V_j(t)$, which allow us to reconstruct the mean velocity profile with the help of a specially designed *PM* basis.

The MZS model conserves the actual integrals of motion of the original NSE of the problem, *energy and linear and angular momenta*; respects Galilean and "asymptotic" scale invariance, the NSE type of nonlinearity; and, in a relatively simple and analytically transparent manner describes the basic physical phenomena in wall-bounded flows for a huge interval of Reynolds numbers. They include (1) the laminar velocity profile for $Re < Re_{cr}$; (2) its instability at $Re = Re_{cr}$; (3) intermediate, nonuniversal mean velocity profile at moderate Re; (4) universal profile for $Re \gg Re_{cr}$ in the viscous sublayer, buffer layer, and logarithmic-law region; (5) spatial distribution of turbulent activity, of the rate of energy dissipations, etc.

The model also allows additional adaptation of the MZS equations for the first few (energy containing) shells to particular flow geometries (like channel, pipe, Couette flows, etc.) which may be based on stability analysis of the laminar regime or some other specific geometrically determined information. This should improve description of the flow for moderate $\mathrm{Re} < 1000$.

The model may also be generalized to the case of viscoelastic turbulent flows (by adding additional shell variables for the polymeric additives), particle laden suspensions, etc.

ACKNOWLEDGMENTS

We thank Itamar Procaccia, Nikolai Nikitin, and Alex Yakhot for useful discussions. The support of the Israel Science Foundation governed by the Israeli Academy of Science is gratefully acknowledged.

APPENDIX A: *PM* BASIS, PROPERTIES, AND INTERPRETATION

1. Construction of the *PM* basis

To construct a "physically motivated" basis for description of the *PM*-velocities, which meets requirements of Sec. III B 1, we consider two subsets of eigenfunctions of the Laplace operator, $\boldsymbol{\phi}_m^+(\boldsymbol{\rho})$ and $\boldsymbol{\phi}_m^-(\boldsymbol{\rho})$, satisfying the incompressibility condition. The no-slip boundary conditions are assumed in the cross section of the flow, with the constraints

$$p_m = (\hat{\mathbf{x}}, \boldsymbol{\phi}_m^+) \neq 0, \tag{A1a}$$

$$\mathcal{R}_m = (\boldsymbol{\mathcal{R}}, \boldsymbol{\phi}_m^-) \neq 0, \tag{A1b}$$

dictated by Eq. (3.2). Notice that both sets $\boldsymbol{\phi}_m^+$ and $\boldsymbol{\phi}_m^-$ are chosen here as real and orthonormal.

Introduce the complex *PM* basis as follows:

$$\boldsymbol{\Phi}_j(\boldsymbol{\rho}) = \sum_{m\in\mathcal{S}_j}\left[p_m\boldsymbol{\phi}_m^+ - i\,\frac{\mathcal{R}_m}{R_j}\,\boldsymbol{\phi}_m^-\right], \tag{A2a}$$

$$m\in\mathcal{S}_j \Leftrightarrow 2^{j-1}\leqslant m\leqslant 2^j-1. \tag{A2b}$$

The normalization "radius" R_j is chosen such that

$$(\boldsymbol{\Phi}_j',\boldsymbol{\Phi}_j') = (\boldsymbol{\Phi}_j'',\boldsymbol{\Phi}_j''), \tag{A3}$$

where

$$\boldsymbol{\Phi}_j'(\boldsymbol{\rho})\equiv \mathrm{Re}[\boldsymbol{\Phi}_j(\boldsymbol{\rho})], \quad \boldsymbol{\Phi}_j''(\boldsymbol{\rho})\equiv \mathrm{Im}[\boldsymbol{\Phi}_j(\boldsymbol{\rho})].$$

Denote

$$s_j\equiv(\boldsymbol{\Phi}_j',\boldsymbol{\Phi}_j') = \sum_{m\in\mathcal{S}_j} p_m^2. \tag{A4}$$

We show below that

$$\sum_{j=1}^{\infty} s_j = 1, \tag{A5}$$

which allows us to understand s_j as a portion of the cross-sectional area, occupied by the j zone. Then, the first of Eqs. (1.10) gives the definition of S_j, the area of the j zone, that is consistent with the requirement $\Sigma_{j=1}^{\infty}S_j = S_\perp$.

To find R_j from Eq. (A3), compute also

$$(\boldsymbol{\Phi}_j'',\boldsymbol{\Phi}_j'') = \frac{1}{R_j^2}\sum_{m\in\mathcal{S}_j}\mathcal{R}_m^2. \tag{A6}$$

Then

$$R_j^2 = s_j^{-1}\sum_{m\in\mathcal{S}_j}\mathcal{R}_m^2. \tag{A7}$$

2. Orthogonality and normalization conditions

By construction (A2), (A3) the *PM* basis is orthogonal in the sense

$$(\boldsymbol{\Phi}_j,\boldsymbol{\Phi}_{j'}) = 2s_j\Delta_{jj'}, \tag{A8a}$$

$$(\boldsymbol{\Phi}_j^*,\boldsymbol{\Phi}_{j'}) = 0. \tag{A8b}$$

The idea behind the choice (A2) is that the functions $\boldsymbol{\Phi}_j'$ and $\boldsymbol{\Phi}_j''$ form the *exact* expansions of the uniform profile of unit height ($\boldsymbol{\Phi}_j'$) and of the linear profile ($\boldsymbol{\Phi}_j''$):

$$\sum_j \boldsymbol{\Phi}_j'(\boldsymbol{\rho}) = \hat{\mathbf{x}}, \tag{A9a}$$

$$\sum_j R_j\boldsymbol{\Phi}_j''(\boldsymbol{\rho}) = -\boldsymbol{\mathcal{R}}. \tag{A9b}$$

These relations can be easily proven by projection of both sides of Eq. (A9) onto the Laplace basis $\phi_m^\pm$, using Eq. (A1) and the definition of the *PM* functions $\boldsymbol{\Phi}_j(\rho)$, Eq. (A2).

Let us show that Eq. (A5) follows from the obvious constraint $(\hat{\mathbf{x}},\hat{\mathbf{x}})=1$, after substitution of $\hat{\mathbf{x}}$ from Eq. (A9a). Using also the orthogonality conditions (A8) one gets

$$\begin{aligned}1 = (\hat{\mathbf{x}},\hat{\mathbf{x}}) &= \sum_{j,j'=1}^{\infty}(\boldsymbol{\Phi}_j',\boldsymbol{\Phi}_{j'}')\\ &= \frac{1}{4}\sum_{j,j'=1}^{\infty}(\boldsymbol{\Phi}_j+\boldsymbol{\Phi}_j^*,\boldsymbol{\Phi}_{j'}+\boldsymbol{\Phi}_{j'}^*)\\ &= \sum_{j=1}^{\infty} s_j.\end{aligned}$$

We proved that all s_j add up to unity according to Eq. (A5).

3. *PM* expansions

Introduce the *PM* projector

$$\begin{aligned}\hat{\mathbf{P}}_{PM}\{\mathbf{f}(\boldsymbol{\rho})\} &= 2\,Re\sum_j\frac{(\boldsymbol{\Phi}_j,\mathbf{f})}{(\boldsymbol{\Phi}_j,\boldsymbol{\Phi}_j)}\boldsymbol{\Phi}_j(\boldsymbol{\rho})\\ &= Re\sum_j s_j^{-1}(\boldsymbol{\Phi}_j,\mathbf{f})\boldsymbol{\Phi}_j(\boldsymbol{\rho}),\end{aligned} \tag{A10}$$

and define the *PM* velocity $\mathbf{V}_{PM}(\boldsymbol{\rho},t)$ as the projection of the full field $\mathbf{V}(\boldsymbol{\rho},t)$ on the *PM* basis:

$$\mathbf{V}_{PM}(\boldsymbol{\rho}) = \hat{\mathbf{P}}_{PM}\{\mathbf{V}(\boldsymbol{\rho})\}. \tag{A11}$$

Using the normalization (A8) one gets Eq. (3.3), in which

$$s_jV_j(t)\equiv(\boldsymbol{\Phi}_j,\mathbf{V}) = (\boldsymbol{\Phi}_j,\mathbf{V}_{PM}). \tag{A12}$$

The expansion coefficients $V_j(t)$ are *PM* velocities in the zone representation.

Substituting $\hat{\mathbf{x}}$ and $\boldsymbol{\mathcal{R}}$ from Eqs. (A9) into the definitions (3.1) of $\mathcal{P}$ and $\mathcal{M}$, one gets with the help of Eqs. (3.3) the *PM* expansion of the linear in $\mathbf{V}$ integrals of motion, Eqs. (3.5). These equation give a proof of the statement that only the *PM* part of the full velocity $\mathbf{V}(\boldsymbol{\rho},t)$, Eq. (3.3), contributes to the mechanical momenta. The turbulent part $\mathbf{V}_T(\boldsymbol{\rho})$ does not contribute to the linear integrals of motion and will be considered as a part of the "turbulent ensemble," described by the shell variables $u_{nj}(t)$.

4. *PM* basis for the channel and pipe flows

In the planar geometry, Fig. 1, $\boldsymbol{\rho}\Rightarrow y$ and the functions $\phi_m^\pm$ in Eq. (A2) are given by

$$\boldsymbol{\phi}_m^+(y) = \hat{\mathbf{x}}\phi_{2m-1}(y),$$

$$\boldsymbol{\phi}_m^-(y) = \hat{\mathbf{z}}\phi_{2m}(y),$$

$$\phi_m(y) = \sqrt{2}\sin(k_m y), \quad k_m = \pi m/(2H), \tag{A13a}$$

$$p_m = \frac{2\sqrt{2}}{\pi(2m-1)} \simeq 0.9/(2m-1). \tag{A13b}$$

For the pipe geometry,

$$\boldsymbol{\phi}_m^+(\rho) = \hat{\mathbf{x}}\phi_m(\rho), \quad \boldsymbol{\phi}_m^-(\rho) = \hat{\mathbf{e}}\phi_m(\rho), \tag{A14a}$$

$$\phi_m(\rho) = J_0(k_m\rho)/J_1(k_m R), \tag{A14b}$$

$$J_0(k_m R) = 0, \quad p_m = 2/(k_m R), \tag{A14c}$$

where $\hat{\mathbf{e}}$ is the polar-angle unit vector ($\hat{\mathbf{e}} \perp \hat{\mathbf{x}}, \hat{\mathbf{e}} \perp \hat{\boldsymbol{\rho}}$), $J_0(\xi)$ and $J_1(\xi)$ are the Bessel functions of the zeroth and first order, and R is the radius of the pipe. The first of Eqs. (A14c) defines $k_m = \xi_m/R$ via zeros of the Bessel functions ξ_m: $J_0(\xi_m) = 0$.

APPENDIX B: EQUATION FOR THE LAMINAR *PM* PROFILE

Here we present a proof that the laminar *PM* profile $\mathbf{V}^0_{PM}(\rho)$ given by Eq. (5.2) satisfies Eq. (5.4).

To this end, we recall that the damping parameters $G_j\kappa_j^2$ are defined as matrix elements:

$$G_j\kappa_j^2 = -s_j^{-1}(\boldsymbol{\Phi}'_j, \Delta\boldsymbol{\Phi}'_j). \tag{B1}$$

Substituting this definition into (5.1),(5.2), we obtain

$$\mathbf{V}^0_{PM}(\boldsymbol{\rho}) = -Re\sum_j \frac{s_j\boldsymbol{\Phi}'_j(\boldsymbol{\rho})}{(\boldsymbol{\Phi}'_j, \Delta\boldsymbol{\Phi}'_j)}. \tag{B2}$$

Then, the Laplacian of $\mathbf{V}^0_{PM}$ is equal to

$$\Delta\mathbf{V}^0_{PM}(\boldsymbol{\rho}) = -Re\sum_j \frac{s_j\Delta\boldsymbol{\Phi}'_j(\boldsymbol{\rho})}{(\boldsymbol{\Phi}'_j, \Delta\boldsymbol{\Phi}'_j)}. \tag{B3}$$

Acting on this Laplacian with the *PM* projector (A10), we obtain

$$\hat{\mathbf{P}}_{PM}\{\Delta\mathbf{V}^0_{PM}\} = -Re\sum_{jk}\frac{s_j}{s_k}\mathrm{Re}\left[\boldsymbol{\Phi}_k\frac{(\boldsymbol{\Phi}_k\Delta\boldsymbol{\Phi}'_j)}{(\boldsymbol{\Phi}'_j, \Delta\boldsymbol{\Phi}'_j)}\right], \tag{B4}$$

where one must distinguish the Reynolds number, *Re*, from the notation for the real part of something, $\mathrm{Re}\{\cdots\}$. Note that by construction different *PM* functions $\boldsymbol{\Phi}_j$ belong to the different subspaces of the eigenfunctions of the Laplace operator. Also, the real $\boldsymbol{\Phi}'_j$ and imaginary $\boldsymbol{\Phi}''_j$ parts of these functions are orthogonal, and thus

$$(\boldsymbol{\Phi}_k, \Delta\boldsymbol{\Phi}'_j) = \Delta_{kj}(\boldsymbol{\Phi}'_j, \Delta\boldsymbol{\Phi}'_j). \tag{B5}$$

As a result, all nondiagonal terms in Eq. (B4) vanish, and we obtain

$$\hat{\mathbf{P}}_{PM}\{\Delta\mathbf{V}^0_{PM}\} = -Re\sum_j \boldsymbol{\Phi}'_j. \tag{B6}$$

Finally, using property (A9a), we obtain

$$\hat{\mathbf{P}}_{PM}\{\Delta\mathbf{V}^0_{PM}\} = -Re\,\hat{\mathbf{x}}, \tag{B7}$$

which actually is Eq. (5.4).

APPENDIX C: WALL-BOUNDED FLOWS IN THE APPROXIMATION OF NEAR-WALL EDDIES ($a=b=c=0$)

In this appendix we analyze the MZS model in the approximation of near-wall eddies, Eqs. (5.8). In the stationary regime ($d/dt=0$) only a finite number $(m-1)\geqslant 0$ of turbulent velocities are nonzero, i.e., $u_j=0$ for $j\geqslant m$. This number depends on *Re*. As it follows from Eq. (5.8a), the *PM* velocities V_j for $j>m$ coincide with the laminar ones:

$$V_j = V_j^0 = \Gamma_j^{-1} \sim 2^{-2j}Re, \quad j>m=m(\mathrm{Re}). \tag{C1}$$

In the unstable region $j<m$, as follows from Eq. (5.8b), the zone velocity difference $\Delta V_j \equiv V_j - V_{j+1}$ coincides with its critical value; see Eq. (5.5):

$$\Delta V_j = \Delta V_j^{\mathrm{cr}} = \frac{2\gamma_j\sigma_j}{d} = A_j/Re,$$

$$A_j \equiv 2g_j\kappa_j^2\sigma_j/d. \tag{C2}$$

This allows one to find all V_j via the last velocity in the unstable region, V_m:

$$V_j = V_m + (B_m - B_j)/Re,$$

$$B_j \equiv \sum_{i=1}^{j-1} A_i. \tag{C3}$$

Multiplying Eq. (5.8a) by s_j and summing up from $j=1$ to $j=m$, one finds the equation for V_m with the solution

$$V_m = \frac{1-\sigma_{m+1}}{C_m}Re - \frac{D_m}{C_m Re}, \tag{C4a}$$

$$C_m \equiv \sum_{j=1}^{m} s_j G_j\kappa_j^2 \sim 2^m, \tag{C4b}$$

$$D_m \equiv \sum_{j=1}^{m} s_j G_j\kappa_j^2(B_m - B_j) \sim 2^{2m}. \tag{C4c}$$

Note that in spite of the large number of different parameters $(A_m, \ldots, D_m)$ all of them are provided with explicit expressions and can be easily evaluated.

Now one finds the total linear mechanical momentum $\mathcal{P}$ (i.e., the total flux of the fluid) of the flow from its definition (4.6b) and Eqs. (C1) and (C4a) for V_j for $j\leqslant m$ and for $j>m$:

$$\mathcal{P} = \sum_{j=1}^{m} s_j V_j + \sum_{j=m+1}^{\infty} s_j V_j^0 = E_m Re + F_m/Re, \tag{C5a}$$

$$E_m \equiv \frac{(1-\sigma_{m+1})^2}{C_m} + \sum_{j=m+1}^{\infty} \frac{s_j}{G_j \kappa_j^2},$$

$$F_m \equiv \sum_{j=1}^{m} s_j (B_m - B_j) - \frac{(1-\sigma_{m+1}) D_m}{C_m}. \qquad \text{(C5b)}$$

So far we treated the last index m in the unstable zones as fixed. However, it depends on the Reynolds number Re and is defined from the condition

$$V_m - V_{m+1} < \Delta V_m^{\rm cr} = \frac{A_m}{Re},$$

which ensures that the turbulent velocity u_m will not be excited, $u_m = 0$. This condition can be written as

$$Re^2 < \frac{A_m C_m + D_m}{1 - \sigma_{m+1} - C_m/(G_{m+1}\kappa_{m+1}^2)} \equiv Re_m^2. \qquad \text{(C6)}$$

Actually, there will be exactly $(m-1)$ excited turbulent velocities u_j, if

$$Re_{m-1} < Re < Re_m. \qquad \text{(C7)}$$

The analysis shows that this condition selects the index m, for which the total momentum $\mathcal{P}$ [Eq. (C5)] has minimum value.

Let us analyze the dependence (C5a) of the total momentum in the limit of extremely large Reynolds numbers, $\ln Re \gg 1$, and, respectively, large critical zone numbers m. In this case we can use the scale invariant limit for all parameters:

$$E_m = 2^{-m}\tilde{E}, \quad F_m = 2^m \tilde{F}, \quad Re_m = 2^m \tilde{R}, \qquad \text{(C8)}$$

where $\tilde{E}$, $\tilde{F}$, and $\tilde{R}$ are some geometry dependent constants. Now for Reynolds numbers inside the range (C7) we can write in Eq. (C5a) $x(Re) = Re/(2^m \tilde{R})$, where $1/2 < x(Re) < 1$. Then $\mathcal{P}$ for large enough Re [in the region of validity of the scale invariant limit (C8)], is given by

$$\mathcal{P}(Re) = x(Re)\tilde{E}\tilde{R} + \frac{\tilde{F}}{x(Re)\tilde{R}}. \qquad \text{(C9)}$$

Since x(Re) is bounded between 1/2 and 1, the flux (C9) is bounded from above by one of the constants

$$\mathcal{P}(Re) \leqslant \max\left\{ \frac{E\tilde{R}}{2} + \frac{2\tilde{F}}{\tilde{R}}, \tilde{E}\tilde{R} + \frac{\tilde{F}}{\tilde{R}} \right\},$$

and does not grow infinitely for infinite Reynolds numbers; see Fig. 6.

APPENDIX D: SOLUTION OF EQS. (5.10)

Consider Eq. (5.10). For $\log_2 Re \gg 1$, in the inertial interval of scales, all needed information contained in Eq. (5.10a) may be obtained from Eq. (4.13) for the momentum flux $\mathfrak{p}_j$, in which one can neglect the damping term $\propto 1/Re$. This gives

$$\mathfrak{p}_j = \frac{du_j^2}{2} = \sum_{j'=1}^{j} s_{j'} = 1 - \sigma_{j+1}, \qquad \text{(D1)}$$

where σ_j is defined by Eq. (4.4c). The substitution of u_j from Eq. (D1) in Eq. (5.11b) gives an expression for V_{j+1} via V_j. This allows one to find V_j for any j outside the viscous region via some constant V_0:

$$V_j = V_0 - \frac{\sqrt{2}\alpha}{d^{3/2}} \sum_{i=1}^{j} \frac{\sigma_i \sqrt{1-\sigma_{i+1}}}{s_i}. \qquad \text{(D2)}$$

For $j > j_*$ (where j_* is equal to, say, 3) one can take in Eq. (D2) $\sigma_j = 2s_j \ll 1$. One concludes that in the inertial interval the *PM* velocities decrease linearly in j:

$$V_j = V_0 + \Delta - \frac{2\sqrt{2}\alpha j}{d^{3/2}}, \quad j > j_*, \qquad \text{(D3a)}$$

$$\Delta = \frac{\sqrt{2}\alpha}{d^{3/2}} \sum_{i=1}^{\infty} \left[2 - \frac{\sigma_i \sqrt{1-\sigma_{i+1}}}{s_i} \right]. \qquad \text{(D3b)}$$

Here the geometry dependent constant Δ was found by comparison of Eqs. (D2) and (D3), and for different geometries it evaluates to

$$\Delta \approx \frac{\alpha}{d^{3/2}} \times \begin{cases} 2.7, & \text{channel}, \\ 2.4, & \text{pipe}. \end{cases} \qquad \text{(D4)}$$

Equation (D3) can be directly obtained from the condition of the constancy of the momentum flux (4.12), which gives

$$u_j = \sqrt{2/d} = \text{const}. \qquad \text{(D5)}$$

Then, in the stationary case, Eq. (5.11b) determines the j independent difference $V_j - V_{j+1}$, necessary for keeping the amplitudes of the near-wall eddies at the constant level. This agrees with Eq. (D3).

In the derivation of Eqs. (D2) and (D3) we cancelled in Eq. (5.10b) $u_j = u_j^*$, assuming that $u_j \neq 0$. At a given Re this assumption is valid only for $j \leqslant j_0$. Here j_0 is the zone index of the last unstable zone, for which in Eq. (5.11b) $d(\ln u_j)/dt > 0$ at $u_j \to 0$. To find j_0 we consider Eq. (5.11b) as an equation for a continuous index q and set its RHS to zero with $u_q = 0$:

$$\frac{g\kappa_q}{Re} = \frac{d}{2}(V_q - V_{q+1}) = \frac{\sqrt{2}\alpha}{\sqrt{d}} \qquad \text{(D6a)}$$

$$\Rightarrow q(Re) = \log_2 Re + \log_2[2 + \sqrt{2}\alpha s/g\sqrt{d}]. \qquad \text{(D6b)}$$

The index j_0 is then the integer part of q.

The solution Eq. (D2) has still an unknown constant, V_0. This constant can be found from the stationarity condition (4.12),

$$\mathfrak{p}^- = \sum_{j=1}^{\infty} s_j \Gamma_j V_j' = \mathfrak{p}^+ = 1, \qquad \text{(D7)}$$

requiring that the total influx of the linear momentum, caused by the pressure gradient, must dissipate at the wall, due to the viscous friction. The product $s_j\Gamma_j \sim 2^j/Re$. Therefore, the sum in Eq. (D7) is dominated by the last few terms with $j \approx j_0 \gg j_*$. This allows one to use the more simple Eq. (D3) instead of Eq. (D2):

$$1 = \frac{G}{4\,Re\;\; s}\sum_{j=1}^{j_0} 2^j\left(V_0+\Delta-\frac{2\sqrt{2}\alpha j}{d^{3/2}}\right) \tag{D8a}$$

$$\approx \frac{G}{2\,Re\;\; s}2^{j_0}\left(V_0+\Delta-\frac{2\sqrt{2}\alpha j_0}{d^{3/2}}\right) \tag{D8b}$$

$$\approx \frac{\sqrt{2}\alpha}{\sqrt{d}}\,\frac{G}{g}\left(V_0+\Delta-\frac{2\sqrt{2}\alpha q(Re)}{d^{3/2}}\right). \tag{D8c}$$

Together with Eq. (D3a) this gives the dependence of V_j on j for the near-wall region, which is geometry independent; see Eq. (5.12).

Notice that in the derivation of Eq. (D2) we neglected in Eq. (5.11b) the viscous damping term $g\kappa_j^2/Re$, with respect to the turbulent one $\alpha|u_j|\kappa_j$. This approximation fails near the viscous cutoff, because $g\kappa_j/Re \propto 2^j$ increases exponentially toward large j, while $\alpha|u_j|$ is approximately constant. More detailed analysis shows that Eq. (D2) fails only for last two j before the cutoff, and instead of a sharp cutoff at $j=j_0$ there is a soft decrease of V_j in two zones near $j=j_0$; see Fig. 8.

APPENDIX E: ITERATION PROCEDURE FOR SOLVING MZS EQUATIONS IN THE EFFECTIVE TURBULENT DAMPING APPROXIMATION

Consider the MZS equations (4.10) for some large Re. As we discussed, there are two regions of j, namely $j<j_{\max}$ and $j \geqslant j_{\max}$. In the "turbulent region," $j<j_{\max}$, the laminar solution, $u_j=0$, is unstable with respect to excitation of turbulent amplitudes u_j and thus, in the stationary regime, $u_j \neq 0$. For $d>0$, without loss of generality all u_j can be taken real and positive definite. In the turbulent region the stationary velocities V_j and u_j satisfy the equations:

$$\Gamma_j V_j = 1 + d\kappa_j(u_{j-1}^2 - u_j^2), \tag{E1a}$$

$$\gamma_j + \alpha\kappa_j u_j = \frac{d}{2\sigma_j}(V_j - V_{j+1}),$$

$$u_j \geqslant 0, \quad j<j_{\max}. \tag{E1b}$$

In the "laminar region" $j \geqslant j_{\max}$:

$$V_j = 1/\Gamma_j, \quad u_j = 0, \quad j \geqslant j_{\max}. \tag{E2}$$

One can substitute V_j from Eq. (E1a) to Eq. (E1b) and get an equation connecting the triad u_{j-1}, u_j, and u_{j+1}. Unfortunately, a direct iteration procedure in this "straightforward" equation is unstable and do not converge to the stationary solution.

To find the stable, stationary solution of Eqs. (E1) numerically, we develop a stable iteration procedure, which is based on the physical understanding of these equations as describing the momentum flux from $j=1$ toward large j in the "interaction triads" V_j, V_{j+1}, and u_j. Denote as $V_j^{(p)}$, $\tilde{V}_{j+1}^{(p)}$, and $u_j^{(p)}$ the solution of following three algebraic equations on the j step in the pth iteration run:

$$\Gamma_j V_j^{(p)} = 1 + d\kappa_j\{[u_{j-1}^{(p)}]^2 - [u_j^{(p)}]^2\},$$

$$\Gamma_{j+1}\tilde{V}_{j+1}^{(p)} = 1 + d\kappa_{j+1}\{[u_j^{(p)}]^2 - [u_{j+1}^{(p-1)}]^2\},$$

$$\gamma_j + \alpha\kappa_j u_j^{(p)} = \frac{d}{2\sigma_j}[V_j^{(p)} - \tilde{V}_{j+1}^{(p)}],$$

$$u_j^{(p)} \geqslant 0 \quad \text{for } j_{\max} > j \geqslant 1, \quad u_0^{(p)} = 0. \tag{E3}$$

As the "initial condition" at $p=0$ we take the (unstable) laminar solution:

$$V_j^{(0)} = \Gamma_j^{-1}, \quad u_j^{(0)} = 0.$$

In the first step, $j=1$, of each iteration run one takes $u_0^{(p)}=0$. Finding $V_1^{(p)}$, $\tilde{V}_2^{(p)}$, and $u_1^{(p)}$ one takes in Eq. (E3) $j=2$, finds $V_2^{(p)}$, $\tilde{V}_3^{(p)}$ and $u_2^{(p)}$ and so on until on some j_0 step one gets negative (or complex) solution for $u_{j_0}^{(p)}$. It means that this amplitude is stable and has to be taken zero, $u_{j_0}^{(p)}=0$. Accordingly, $j_0 = j_{\max}$. For all $j>j_{\max}$ one takes the laminar solution: $V_j^{(p)} = 1/\Gamma_j$, $u_j^{(p)}=0$.

After that one begin the next, $p+1$, iteration run, starting again from its first step, $j=1$. It can be shown, that the velocities $V_1^{(p)}$ form a monotonically decreasing sequence with increasing p and are always positive. Since a limited from below, monotonically decreasing sequence always have some finite limit, this proves the convergence and stability of our iteration scheme. The calculations show that for Reynolds numbers $Re \leqslant 10^9$ the velocities V_j and u_j converge (with accuracy about 10^{-6}) after 100–200 iteration runs.

[1] E. B. Gledzer, Dokl. Akad. Nauk SSSR **200**, 1043 (1973).

[2] M. Yamada and K. Ohkitani, J. Phys. Soc. Jpn. **56**, 4210 (1987).

[3] V. S. L'vov, E. Podivilov, A. Pomyalov, I. Procaccia, and D. Vandembroucq, Phys. Rev. E **58**, 1811 (1998).

[4] T. Bohr, M. Jensen, G. Paladin, and A. Vulpiani, *Dynamical Systems Approach to Turbulence* (Cambridge University Press, Cambridge, England, 1998).

[5] L. Biferale, Annu. Rev. Fluid Mech. **35**, 441 (2003), and references therein.

[6] V. Zimin and F. Hussain, Phys. Fluids **7**, 2925 (1995).

[7] P. Frick and V. Zimin, in *Wavelets, Fractals and Fourier*

Transforms (Clarendon, Oxford, 1993).
[8] C. Meneveau, J. Fluid Mech. **232**, 469 (1991).
[9] T. Nakano, Phys. Fluids **31**, 1420 (1988).
[10] E. Aurell, P. Frick, and V. Shaidurov, Physica D **72**, 95 (1994).
[11] R. Benzi, L. Biferale, R. Tripiccione, and E. Trovatore, Phys. Fluids **9**, 2355 (1996).
[12] S. B. Pope, *Turbulent Flows* (Cambridge University Press, Cambridge, England, 2000).
[13] J. L. Lumley, Adv. Appl. Mech. **18**, 123 (1978).
[14] A. S. Monin and A. M. Yaglom, *Statistical Fluid Mechanics of Turbulence* (MIT Press, Cambridge, MA, 1975), Vol. 2.
[15] V. Yakhot and S. A. Orszag, J. Sci. Comput. **1**, 3 (1986).
[16] V. Yakhot, S. A. Orszag, S. Thangam, T. B. Gatski, and C. G. Speziale, Phys. Fluids A **4**, 1510 (1992).
[17] L. M. Smith and W. C. Reynolds, Phys. Fluids A **4**, 364 (1992).
[18] M. Holschneider, *Wavelets, an Analysis Tool* (Clarendon, Oxford, 1995).
[19] E. De Angelis, C. M. Casciola, V. S. L'vov, R. Piva, and I. Procaccia, Phys. Rev. E **67**, 056312 (2003).
[20] M. V. Zagarola and A. J. Smits, Phys. Rev. Lett. **78**, 239 (1997).
[21] N. N. Mansour, J. Kim, and P. Moin, J. Fluid Mech. **194**, 15 (1998).
[22] V. Zimin (private communication).